

# D<sup>3</sup>-Predictor: Noise-Free Deterministic Diffusion for Dense Prediction

Changliang Xia\*    Chengyou Jia\*    Minnan Luo<sup>†</sup>    Zhuohang Dang    Xin Shen  
 Bowen Ping

School of Computer Science and Technology, Xi'an Jiaotong University

202066@stu.xjtu.edu.cn, cp3jia@stu.xjtu.edu.cn, minnluo@xjtu.edu.cn,  
 dangzhuohang@stu.xjtu.edu.cn, 2213311110@stu.xjtu.edu.cn, jayceping6@gmail.com

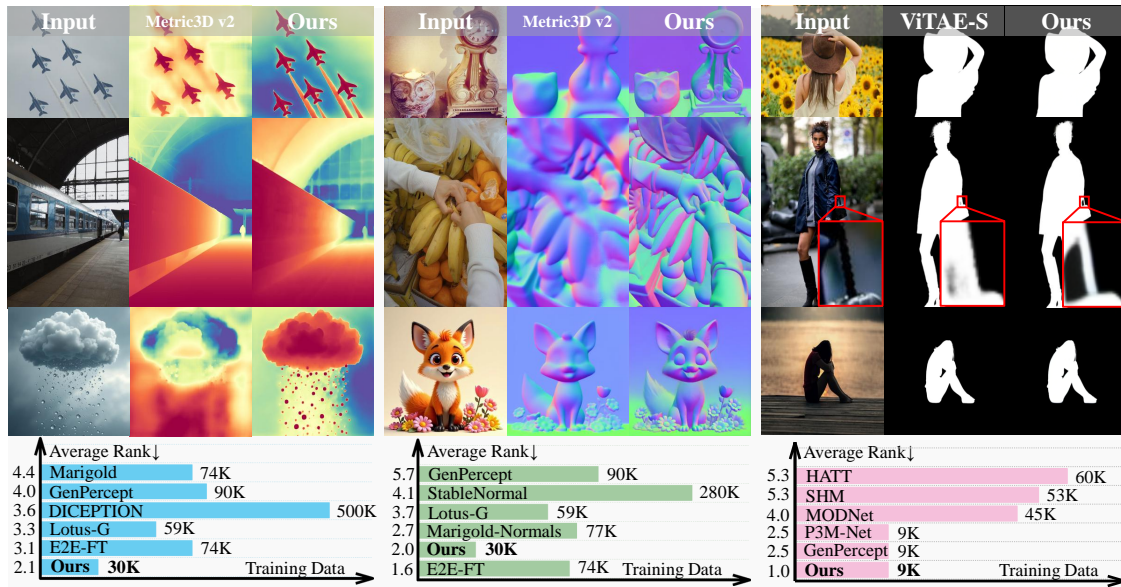


Figure 1. We present D<sup>3</sup>-Predictor, a noise-free deterministic diffusion model achieving superior performance and generalization across various dense prediction tasks, with less than half the training data previously used and efficiently performing inference in a single step.

## Abstract

Although diffusion models with strong visual priors have emerged as powerful dense prediction backbones, they overlook a core limitation: the stochastic noise at the core of diffusion sampling is inherently misaligned with dense prediction that requires a deterministic mapping from image to geometry. In this paper, we show that this stochastic noise corrupts fine-grained spatial cues and pushes the model toward timestep-specific noise objectives, consequently destroying meaningful geometric structure mappings. To address this, we introduce **D<sup>3</sup>-Predictor**, a noise-free deterministic diffusion-based dense prediction model built by reformulating a pretrained diffusion model without stochastic noise. Instead of relying on noisy inputs to leverage diffusion priors, D<sup>3</sup>-Predictor views the pretrained dif-

fusion network as an ensemble of timestep-dependent visual experts and self-supervisedly aggregates their heterogeneous priors into a single, clean, and complete geometric prior. Meanwhile, we utilize task-specific supervision to seamlessly adapt this noise-free prior to dense prediction tasks. Extensive experiments on various dense prediction tasks demonstrate that D<sup>3</sup>-Predictor achieves competitive or state-of-the-art performance in diverse scenarios. In addition, it requires less than half the training data previously used and efficiently performs inference in a single step. Our code, data, and checkpoints are publicly available at [https://x-gengroup.github.io/HomePage\\_D3-Predictor/](https://x-gengroup.github.io/HomePage_D3-Predictor/).

## 1. Introduction

Dense prediction, such as depth estimation [50] and surface normal estimation [76], are fundamental tasks in computer vision, with numerous applications like autonomous

\*Equal Contribution

<sup>†</sup>Corresponding Author

driving [6, 20], scene reconstruction [10, 90], inverse rendering [9, 87], and so on. Although state-of-the-art discriminative dense prediction models [4, 25] achieve impressive performance, they still struggle to capture fine-grained high-frequency details. To address this limitation, current works [17, 31, 41, 84, 92] reformulate dense prediction as an image-conditioned iterative denoising process based on diffusion models [66]. By leveraging powerful visual priors of diffusion models, these methods can produce dense predictions results with fine-grained geometric details.

While these diffusion-based dense prediction methods have demonstrated promising results, they still suffer from the stochastic noise inherent in diffusion models. Stochastic noise is a fundamental component of diffusion models, enabling sample diversity that is particularly beneficial for creative image [44, 58, 79] and video [75, 83, 91] generation. However, dense prediction is intrinsically deterministic, indicating that the **stochastic noise essential to diffusion models may be misaligned with the task’s deterministic objective**. We posit that the stochastic noise introduces two critical issues for dense prediction tasks: 1) Stochastic noise disrupts the geometric structures and small-scale objects in the input image, thereby degrading the integrity of input information and impeding precise spatial perception (cf. Fig. 2 (a)); 2) The stochastic noise drives diffusion models to focus on modeling noise distributions [24] instead of establishing the geometric structure mappings essential for dense prediction tasks [17]. Moreover, the iterative denoising process of the diffusion model further incurs substantial inference overhead. These observations motivate a fundamental question: **Can diffusion models be reformulated into a noise-free deterministic framework to better suit dense prediction tasks?**

Recent works attempt to employ deterministic noise to alleviate the stochasticity in diffusion-based dense prediction methods. For example, GenPercept [80] and E2E-FT [18] eliminate stochasticity by fixing the noise schedule (a function of the timestep) to introduce deterministic noise. However, diffusion models learn timestep-specific objectives [2, 3], leading to distinct diffusion priors at each timestep. Consequently, fixing the noise schedule disrupts this prior structure, resulting in incomplete priors and a loss of geometric fidelity (cf. Fig. 2 (b)). On the other hand, StableNormal [84] suppresses stochasticity while preserving diffusion priors via a more complex two-stage pipeline with external DINO [55] guidance. However, this design incurs a higher computational overhead.

In this work, we aim to fully eliminate the adverse effects of stochastic noise on diffusion-based dense prediction, without compromising the diffusion prior and with minimal additional computational cost. To this end, we propose **D<sup>3</sup>-Predictor**, a noise-free deterministic diffusion-based dense prediction model initialized from the pretrained

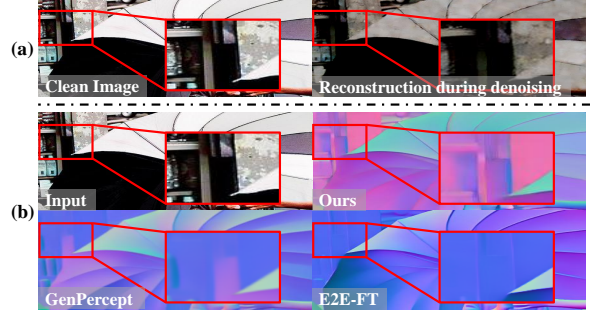


Figure 2. (a) Stochastic noise regarding the integrity of input information; (b) Current attempts to alleviate the stochasticity lead to a loss of geometric fidelity.

diffusion model. Specifically, we treat the pretrained diffusion models at different timesteps as an ensemble of visual experts following the CleanDIFT [70] paradigm, each exhibiting distinct timestep-dependent diffusion priors. In this context, each visual expert takes a noisy image together with its timestep as input, while our D<sup>3</sup>-Predictor operates directly on a clean image. D<sup>3</sup>-Predictor then aggregates diffusion priors from multiple visual experts into a complete and noise-free one in a lightweight self-supervised manner, by aligning its internal representations with those of visual experts. We simultaneously apply task-specific supervision to the D<sup>3</sup>-Predictor to easily leverage this aggregated diffusion prior for various dense prediction tasks.

We conduct extensive experiments across multiple dense prediction tasks. The results show that our noise-free D<sup>3</sup>-Predictor achieves competitive or state-of-the-art performance across diverse zero-shot benchmarks. More importantly, D<sup>3</sup>-Predictor markedly improves both training and inference efficiency of diffusion-based dense prediction methods, allowing the model to train with less than half of the data previously required (cf. Fig. 1) and to efficiently perform inference in a single step. We believe that D<sup>3</sup>-Predictor paves a promising path toward reformulating powerful diffusion models for dense prediction.

Our main contributions can be summarized as follows:

- We introduce D<sup>3</sup>-Predictor, an end-to-end noise-free deterministic diffusion-based dense prediction model. D<sup>3</sup>-Predictor combines self-supervised noise-free diffusion prior aggregation with task-specific supervision, allowing the model to transfer the diffusion priors into a noise-free geometric prior specifically for dense prediction tasks.
- Our D<sup>3</sup>-Predictor fully eliminates noise in diffusion-based dense prediction, successfully preserving complete diffusion priors with minimal additional computational cost.
- Extensive experiments on various dense prediction tasks demonstrate that our noise-free D<sup>3</sup>-Predictor achieves competitive or state-of-the-art performance. It also improves training and inference efficiency while preserving high geometric fidelity of the predicted results.

## 2. Related Work

### 2.1. Diffusion-based Dense Prediction

Several works have explored leveraging diffusion models for dense prediction. Methods such as DIFT [71] and CleanDIFT [70] extract diffusion priors as general-purpose visual features and train lightweight probes for dense prediction tasks, but they are not end-to-end and their performance remains limited. While CleanDIFT [70] obtains noise-free general-purpose features, our method integrates this mechanism with task-specific supervision in an end-to-end manner. This joint optimization allows us to effectively transform the aggregated diffusion priors into noise-free geometric priors specifically tailored for dense prediction. On the other hand, other methods [17, 21, 31, 92] fine-tune a pre-trained diffusion model for dense prediction tasks, achieving impressive results. However, these fine-tuning methods rely on stochastic noise to exploit diffusion priors. GenPercept [80] and E2E-FT [18] attempt to alleviate stochasticity but disrupt the integrity of diffusion priors, while StableNormal [84] suppresses stochasticity at the cost of additional computational overhead. In contrast, our method reformulates the diffusion model into a noise-free framework to better suit dense prediction in a simple self-supervised manner, ensuring both prediction performance and speed.

### 2.2. Self-Supervised Enhanced Diffusion Models

Recent studies [28, 78, 86] have shown that enhancing the internal representations of diffusion models, which serve as diffusion priors, can accelerate generative training and improve generation quality. Unlike methods [86] that rely on external pretrained features (e.g., DINO [55]), SRA [28] improves diffusion representations in a self-supervised way via self-representation alignment. The self-supervised enhancement in SRA [28] leads to improvements in both image generation quality and efficiency, demonstrating that diffusion models can provide representation guidance by themselves. In this work, we extend the idea of this self-supervised enhancement from diffusion-based generation to diffusion-based dense prediction. We align the noise-free internal representations of the diffusion model with their noisy counterparts at different noise levels in a self-supervised manner. This process produces complete, noise-free diffusion priors that are inherently more suitable for dense prediction.

## 3. Method

### 3.1. Preliminary: Diffusion-based Dense Prediction

In general, a diffusion model consists of an autoencoder and a denoising network. The autoencoder converts an image  $y \in \mathbb{R}^{H \times W \times 3}$  into  $z^{(y)} \in \mathbb{R}^{h \times w \times d}$ , where  $(h, w)$  denote the latent spatial dimensions and  $d$  is the latent channel di-

mension. The diffusion process then gradually corrupts the latent code  $z^{(y)}$  over multiple timesteps by adding noise:

$$z_t^{(y)} = \sqrt{\alpha_t} z^{(y)} + \sqrt{1 - \alpha_t} \epsilon, \quad (1)$$

where  $\epsilon \sim \mathcal{N}(0, I)$  is the noise, and  $\alpha_t$  is the noise schedule (a function of the timestep  $t$ ). The denoising network then learns to iteratively reverse this process conditioned on the inputs  $c$  (e.g., text prompts), to recover the original latent code from the noisy version.

As illustrated in Fig. 3 (b), previous diffusion-based dense prediction methods, such as Marigold [31], adopt the time-consuming iterative denoising process described above, where the conditional input  $c$  is an RGB image. At each iteration, the model progressively removes stochastic noise associated with a specific noise level and timestep, thus necessitating multi-step inference.

In contrast, recent work GenPercept [80] simplifies this process by fixing the noise schedule. However, it is worth noting that diffusion models have different objectives at different noise levels [2, 3]. At higher noise levels, the model captures coarse structural information, while at lower noise levels, it focuses on details [64]. Thus, the model learns distinct diffusion priors across timesteps, which together constitute a complete diffusion prior. Fixing the noise schedule disrupts this prior structure, leading to incomplete priors and suboptimal performance.

Based on these observations, our method aggregates the diffusion priors across timesteps into a noise-free and complete one, which not only preserves the integrity of the diffusion prior but also achieves superior performance through efficient single-step inference.

### 3.2. D<sup>3</sup>-Predictor

We aim to reformulate diffusion models into a noise-free framework when applied to dense prediction, without compromising diffusion priors with minimal overhead. To this end, we propose D<sup>3</sup>-Predictor, a noise-free deterministic diffusion-based dense prediction model, as shown in Fig. 3.

#### 3.2.1. Self-Supervised Diffusion Priors Aggregation

The core of our approach is to train our D<sup>3</sup>-Predictor  $f_{D^3}(\cdot)$  to incorporate a noise-free and complete diffusion prior compared to the pre-trained diffusion model, which is enhanced to be more suitable for deterministic dense prediction tasks. We achieve this enhancement through a simple self-supervised manner, and crucially, relying solely on the model itself rather than costly external guidance (e.g., DINO [55]) adapted by previous works [84]. We begin by initializing D<sup>3</sup>-Predictor with a pretrained diffusion model.

As shown in Fig 3 (a), the insight here is to view the diffusion model as an ensemble of  $t$  visual experts, where each expert  $f_{\text{exp}}(\cdot, \epsilon, t)$  exhibits a distinct timestep-dependent diffusion prior. We inherit the mechanism of aligning a

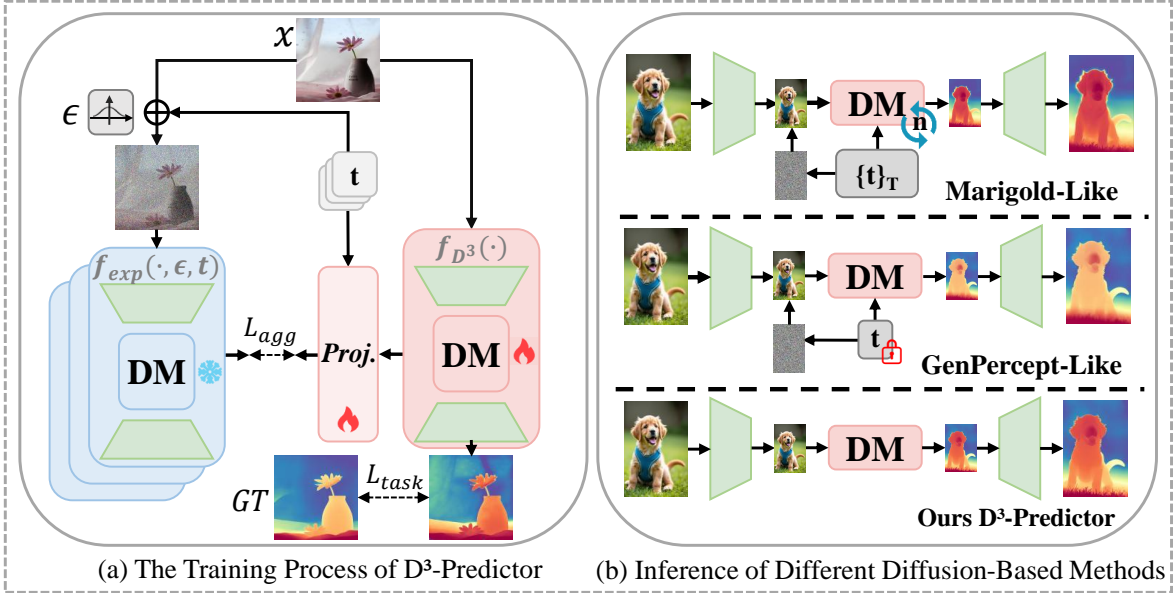


Figure 3. Overview of the D<sup>3</sup>-Predictor. (a) We reformulate the pretrained diffusion model into a noise-free framework to better suit dense prediction tasks, without compromising the diffusion prior with minimal overhead. (b) The D<sup>3</sup>-Predictor takes a clean image as input and produces an accurate prediction with impressive geometric details in a single step.

clean backbone with a frozen diffusion model from CleanDIFT [70]. While the visual experts take a noisy image  $(\epsilon, x)$  together with its timestep  $t$  as input, our D<sup>3</sup>-Predictor operates directly on a clean image  $x$ . During training, D<sup>3</sup>-Predictor aligns its internal representations  $r_{D^3}^K = f_{D^3}^K(x)$  with those of  $t$  visual experts  $r_{\text{exp}}^{K,t} = f_{\text{exp}}^K(x, \epsilon, t)$ . Here,  $K$  is the index set of model layers selected for alignment.

To stabilize this timestep-dependent representation alignment, we introduce a lightweight, trainable timestep-conditioned projection head  $P_\varphi^K(\cdot, t)$  parameterized by  $\varphi$ . While the use of projection heads for representation alignment has proven effective in prior works [28, 70, 78, 86], we specifically leverage the timestep-conditioned projection head adopted by CleanDIFT [70] and shown in Fig 3 (a). This projection head serves to project the single, noise-free representation  $r_{D^3}^K$  into  $T$  distinct timestep-dependent representation spaces for the purpose of matching the expert representations. This mechanism implicitly requires our model’s representation to encode the diverse diffusion priors corresponding to different noise levels. We measure the alignment by their point-wise distance:

$$L_{\text{agg}} = \sum_{t \in T} \sum_{k \in K} \text{dist}(r_{\text{exp}}^{k,t}, P_\varphi^k(r_{D^3}^k, t)), \quad (2)$$

Where  $\text{dist}(\cdot, \cdot)$  denotes a predefined distance function. By minimizing  $L_{\text{agg}}$ , our D<sup>3</sup>-Predictor obtains a noise-free and complete internal representation that aggregates diffusion model’s timestep-dependent priors into a single one, which is more suitable for deterministic dense prediction tasks.

### 3.2.2. Task-Specific Supervision

We meanwhile apply task-specific supervision by minimizing the task-specific loss  $L_{\text{task}}$  to the D<sup>3</sup>-Predictor to leverage this aggregated diffusion prior for dense prediction tasks. For depth estimation,  $L_{\text{task}}$  is defined as a weighted sum of the MSE loss, the affine-invariant loss [60], and the gradient loss in log space [60]. For surface normal estimation,  $L_{\text{task}}$  is defined as a weighted sum of the MSE loss and the angular loss. For image matting,  $L_{\text{task}}$  is defined as a weighted sum of the MSE loss,  $\ell_1$  loss, and gradient loss. Notably, the task-specific supervision and the self-supervised diffusion priors aggregation are jointly optimized. As a result, the aggregated diffusion prior preserves more task-relevant geometric structure information while suppressing irrelevant color-related information. Finally, the overall training objective  $L$  is defined as:

$$L = L_{\text{agg}} + \lambda L_{\text{task}}, \quad (3)$$

where  $\lambda > 0$  is a hyperparameter that balances the self-supervised and supervised training objectives.

During inference, the D<sup>3</sup>-Predictor takes a clean image as the sole input and generates an accurate prediction result with impressive geometric details in a single step, as illustrated in Fig. 3 (b). More details (e.g., calculation details of  $L_{\text{task}}$  for different tasks) can be found in the Appendix.

### 3.3. Training on Mixed Data

The quality of real dense prediction datasets suffer from the physical limitations of sensing devices [26]. Recent dense prediction methods [31, 80, 92] have instead opted to train

entirely on synthetic datasets. However, we argue that the domain gap between synthetic and real data can hinder real-world generalization. In this work, we train our model on a balanced mixture of synthetic data and real images with pseudo labels. The synthetic data provide fine-grained geometric details, whereas the real images contribute to the model’s generalization by providing more diverse scenes.

## 4. Experiments

### 4.1. Experimental Settings

#### 4.1.1. Training Datasets

We train D<sup>3</sup>-Predictor on different datasets for different dense prediction tasks: 1) For depth estimation: we use 10,777 samples from Hypersim [65], a synthetic indoor scene dataset; 4,252 samples from Virtual KITTI [6], a synthetic driving scene dataset; and 15,160 real images from COCO [45] with pseudo-depth labels generated by Depth Pro [4]. 2) For surface normal estimation: we use 29,284 samples from Hypersim [65] and 376 samples from Sintel [5], which contains both indoor and outdoor scenes from a short animated film. 3) For image matting: we use the training set of P3M-10K [43], which includes 9,421 images and is currently the largest portrait matting dataset. We only employ real images with pseudo labels for depth estimation, since other tasks have been less explored and their models generalize poorly to in-the-wild images. More details on the training data (e.g. data mixing strategies) are in Appendix.

#### 4.1.2. Implementation Details

Unless otherwise specified, we initialize our D<sup>3</sup>-Predictor with Stable Diffusion v2.1 [66] for fair comparison with previous works that also adopt it. We fine-tune the U-Net of it using an image resolution of  $768 \times 768$ . We employ the Adam optimizer [46] with a batch size of 32 and a learning rate of  $1e-5$ , following a linear warm-up schedule. All experiments are conducted on two NVIDIA L40S GPUs.

## 4.2. Comparison to the state-of-the-art

### 4.2.1. Depth Estimation

Depth estimation predicts the distance between the object and the camera from an image. We perform evaluations on five zero-shot real-world benchmarks, including NYUv2 [69], KITTI [19], ETH3D [67], ScanNet [13], and DIODE [73]. The evaluation metrics include the Absolute Mean Relative Error (RelAbs) and the  $\delta_1$ -accuracy.

We compare specialized discriminative models [25], multi-task models [40], and diffusion-based models [31]. Table 1 presents the quantitative comparison results. D<sup>3</sup>-Predictor demonstrates remarkable zero-shot generalization and promising performance across five benchmarks. Compared with diffusion-based methods, D<sup>3</sup>-Predictor requires neither multi-step sampling nor test-time ensem-

bling, thereby achieving significantly higher inference efficiency and stability without sacrificing accuracy. Although our model lags behind state-of-the-art discriminative models in terms of quantitative performance, it produces visually sharper results, as shown in Fig. 4. When encountering out-of-domain scenes (e.g., AIGC-generated images), the performance of discriminative models drops drastically. Notably, most discriminative models require large-scale datasets and complex data pipelines, while our model only relies on limited synthetic data and arbitrary real images.

### 4.2.2. Surface Normal Estimation

Surface normal estimation predicts the direction vector perpendicular to the surface at each point on the object. We perform evaluations on five zero-shot real-world benchmarks, including NYUv2 [69], ScanNet [13], iBims-1 [36], DIODE [73] and OASIS [8]. The evaluation metrics include mean angular error and the percentage of pixels with an angular error below the threshold of  $11.25^\circ$ .

We compare specialized discriminative models [25] and diffusion-based models [32]. The quantitative results in Table 2 reveal that our D<sup>3</sup>-Predictor is competitive with state-of-the-art diffusion-based models across five benchmarks, while also demonstrating impressive inference efficiency and stability. Although E2E-FT [18] achieves marginally better performance than D<sup>3</sup>-Predictor, our model is significantly more data-efficient, requiring less than half of its training data. This is particularly advantageous in real-world applications, where annotating large-scale dense labels and training diffusion models is costly and thus often limits deployment. Fig. 4 further highlights the geometric detail generation capability and robustness of our approach.

### 4.2.3. Image Matting

Image matting aims to extract the foreground and background from an image and generate an alpha matte. We evaluate our method on the P3M-500-NP test set [43]. The evaluation metrics include the sum of absolute differences (SAD), mean squared error (MSE), mean absolute difference (MAD) and connectivity (Conn.).

Table 3 presents the quantitative comparison results. Overall, our method significantly outperforms a recent diffusion-based method GenPercept [80], demonstrating the superiority of our D<sup>3</sup>-Predictor for image matting. Moreover, compared with state-of-the-art discriminative matting models, D<sup>3</sup>-Predictor achieves clearly competitive performance. Qualitative comparisons in Fig. 5 further show that our method produces high-quality alpha mattes, especially in challenging regions such as transparent area and hair.

### 4.2.4. Generalization to Domain-Specific Tasks

To further assess the generalization and practical utility of our D<sup>3</sup>-Predictor, we evaluate it on 20 additional domain-specific dense prediction tasks, such as medical image anal-

Table 1. Quantitative comparison of different depth estimation methods across multiple zero-shot benchmarks. We use the same evaluation protocol as DCEPTION [92]. NFEs is the numbers of function evaluations (ensemble  $\times$  steps)

Method	Training Samples	NFEs	KITTI		NYU		ScanNet		DIODE		ETH3D		Average Rank $\downarrow$
			AbsRel $\downarrow$	$\delta_1 \uparrow$									
MiDaS [60]	2M	-	0.236	0.630	0.111	0.885	0.121	0.846	0.332	0.715	0.184	0.752	6.9
Omnidata [14]	12.2M	-	0.149	0.835	0.074	0.945	0.075	0.936	0.339	0.742	0.166	0.778	5.1
DPT-large [61]	1.4M	-	0.100	0.901	0.098	0.903	0.082	0.934	0.182	0.758	0.078	0.946	4.2
DiverseDepth [85]	320K	-	0.190	0.704	0.117	0.875	0.109	0.882	0.376	0.631	0.228	0.694	7.0
HDN [88]	300K	-	0.115	0.867	0.069	0.948	0.080	0.939	0.246	0.780	0.121	0.833	3.9
DepthAnything [81]	63.5K	-	0.080	0.946	0.043	<b>0.980</b>	0.043	0.981	0.261	0.759	0.058	<b>0.984</b>	2.2
DepthAnything v2 [82]	62.6M	-	0.080	0.943	0.043	0.979	0.042	0.979	0.321	0.758	0.066	0.983	2.8
Metric3D v2 [25]	16M	-	<b>0.052</b>	<b>0.979</b>	<b>0.039</b>	0.979	<b>0.023</b>	<b>0.989</b>	<b>0.147</b>	<b>0.892</b>	<b>0.040</b>	0.983	<b>1.2</b>
Unified-IO [47]	48K	-	0.188	0.699	<b>0.059</b>	<b>0.970</b>	<b>0.063</b>	<b>0.965</b>	0.369	<b>0.906</b>	0.103	0.906	1.9
4M-XL [51]	759M	-	0.105	0.896	0.068	0.951	0.065	0.955	<b>0.331</b>	0.734	<b>0.070</b>	<b>0.953</b>	<b>1.7</b>
OneDiffusion [40]	500K	-	<b>0.101</b>	<b>0.908</b>	0.087	0.924	0.094	0.906	0.399	0.661	0.072	0.949	2.4
Marigold [31]	74K	$10 \times 50$	0.099	0.916	0.055	0.964	0.064	0.951	0.308	0.773	0.065	0.960	4.4
DMP [41]	10K	$1 \times 5$	0.240	0.622	0.109	0.891	0.146	0.814	0.361	0.706	0.128	0.857	7.7
DepthFM [21]	63K	$10 \times 4$	0.174	0.718	0.082	0.932	—	—	<b>0.225</b>	<b>0.800</b>	—	—	5.2
Deception [92]	500K	$1 \times 28$	<b>0.075</b>	<b>0.945</b>	0.072	0.939	0.075	0.938	<u>0.243</u>	0.741	<b>0.053</b>	<b>0.967</b>	3.6
GeoWizard [17]	280K	$10 \times 50$	0.129	0.851	0.059	0.959	0.066	0.953	0.328	0.753	0.077	0.940	5.6
Lotus-G [23]	59K	$1 \times 1$	0.113	0.877	<u>0.054</u>	<u>0.966</u>	0.060	0.960	—	—	<u>0.062</u>	<u>0.961</u>	3.3
E2E-FT [18]	74K	$1 \times 1$	0.096	0.921	<u>0.054</u>	0.965	<u>0.058</u>	<b>0.965</b>	0.303	0.776	0.064	0.959	<u>3.1</u>
Genpercept [80]	90K	$1 \times 1$	0.094	0.923	0.091	0.932	<b>0.056</b>	<b>0.965</b>	0.302	0.767	0.066	0.957	4.0
Ours	30K	$1 \times 1$	<u>0.082</u>	<u>0.940</u>	<b>0.052</b>	<b>0.970</b>	0.063	<u>0.963</u>	0.290	<u>0.779</u>	0.062	<u>0.961</u>	<b>2.1</b>

Table 2. Quantitative comparison of different surface normal estimation methods across multiple zero-shot benchmarks. We use the same evaluation protocol as Marigold-Normals [32]. NFEs is the numbers of function evaluations (ensemble  $\times$  steps).

Method	Training Samples	NFEs	NYUv2		ScanNet		iBims-1		DIODE		OASIS		Average Rank $\downarrow$
			Mean $\downarrow$	11.25° $\uparrow$									
DSINE [1]	160K	-	0.164	0.596	<b>0.162</b>	<b>0.610</b>	<b>0.171</b>	0.674	0.199	0.418	0.244	<b>0.288</b>	1.7
Omnidata v2 [30]	12.2M	-	0.172	0.555	<b>0.162</b>	0.602	0.182	0.639	0.206	0.408	0.242	0.277	2.5
Metric3D v2 [25]	16M	-	<b>0.133</b>	<b>0.664</b>	—	—	0.196	<b>0.697</b>	<b>0.126</b>	<b>0.649</b>	<b>0.234</b>	0.285	<b>1.4</b>
GeoWizard [17]	280K	$10 \times 50$	0.190	0.500	0.176	0.546	0.193	0.623	0.247	0.301	0.253	0.269	6.0
StableNormal [84]	280K	$1 \times 10$	0.178	0.542	0.167	0.540	<u>0.171</u>	0.678	<u>0.193</u>	<b>0.538</b>	0.257	0.254	4.1
Marigold-Normals [32]	77K	$1 \times 1$	<u>0.164</u>	<u>0.589</u>	<u>0.149</u>	<u>0.643</u>	0.172	0.656	0.195	0.432	<b>0.232</b>	<b>0.283</b>	2.7
Lotus-G [23]	59K	$1 \times 1$	0.169	0.591	0.153	<u>0.640</u>	0.174	0.661	0.212	0.397	0.247	0.270	3.7
E2E-FT [18]	74K	$1 \times 1$	0.165	<b>0.604</b>	<b>0.147</b>	<b>0.661</b>	<b>0.161</b>	<b>0.697</b>	<b>0.190</b>	0.444	<u>0.236</u>	<u>0.279</u>	<b>1.6</b>
Genpercept [80]	44K	$1 \times 1$	0.183	0.560	0.182	0.574	0.183	0.638	0.223	0.381	0.259	0.233	5.7
Ours	30K	$1 \times 1$	<b>0.162</b>	<u>0.595</u>	0.153	0.618	<b>0.161</b>	<u>0.687</u>	<b>0.190</b>	0.472	<b>0.232</b>	0.276	<u>2.0</u>

Table 3. Evaluation of image matting on P3M-500-NP test set.

Method	Training Samples	SAD $\downarrow$	MAD $\downarrow$	MSE $\downarrow$	CONN $\downarrow$	Average Rank $\downarrow$
HATT [57]	60K	30.35	0.0176	0.0072	27.42	4.8
SHM [7]	53K	20.77	0.0122	0.0093	17.09	4.3
MODNet [33]	45K	16.70	0.0097	0.0051	13.81	3
P3M-Net [43]	9K	11.23	0.0065	0.0035	12.51	2
ViTAE-S [49]	9K	<b>7.59</b>	<b>0.0044</b>	<b>0.0019</b>	<b>6.96</b>	<b>1</b>
GenPercept [80]	9K	12.77	0.0074	0.0027	10.46	2
Ours	9K	<b>7.97</b>	<b>0.0046</b>	<b>0.0015</b>	<b>7.43</b>	<b>1</b>

ysis. These tasks are typically constrained by data scarcity, often due to factors like privacy protection. For these evaluations, we train our model using only 15 samples per task with a simple MSE loss. We present *Spinal Morphology Assessment* source from [12] as a representative example.

As summarized in Table 4, D<sup>3</sup>-Predictor significantly outperforms strong zero-shot baselines, such as SAM [35], by over **60%** in average performance, demonstrating its superior generalization in the medical domain. The qualitative results in Fig. 6 further show our model accurately captures

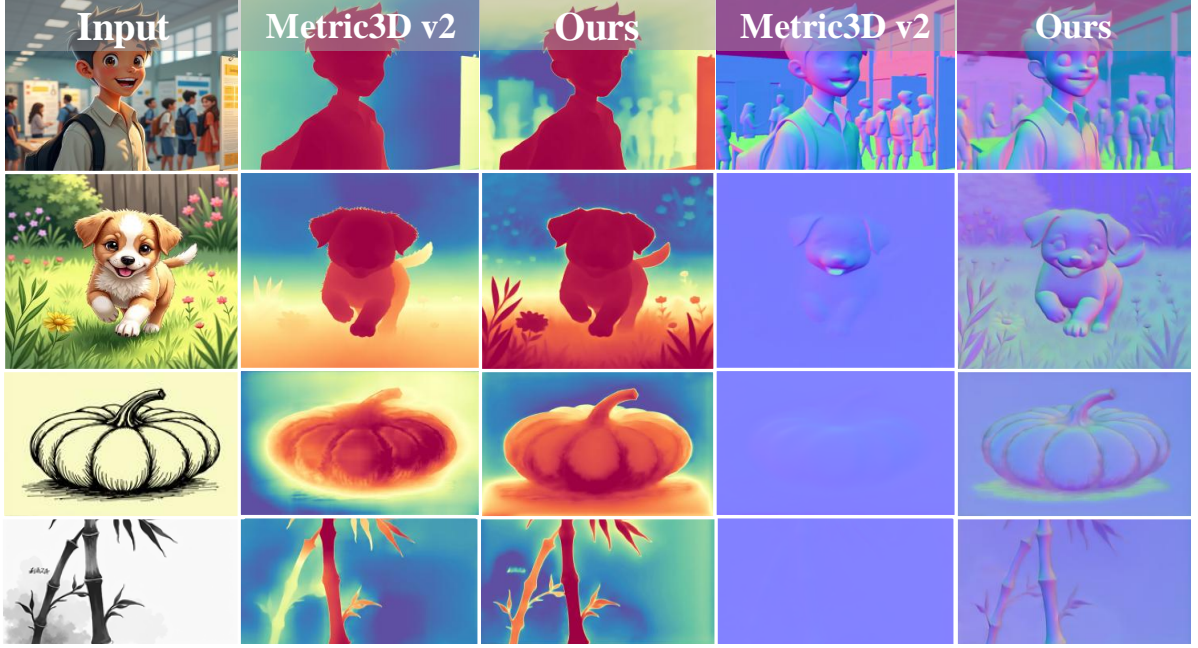


Figure 4. Comparison of geometric detail generation capability on out-of-domain scenes. State-of-the-art discriminative models show significant performance degradation on out-of-domain images, while our model works surprisingly well.

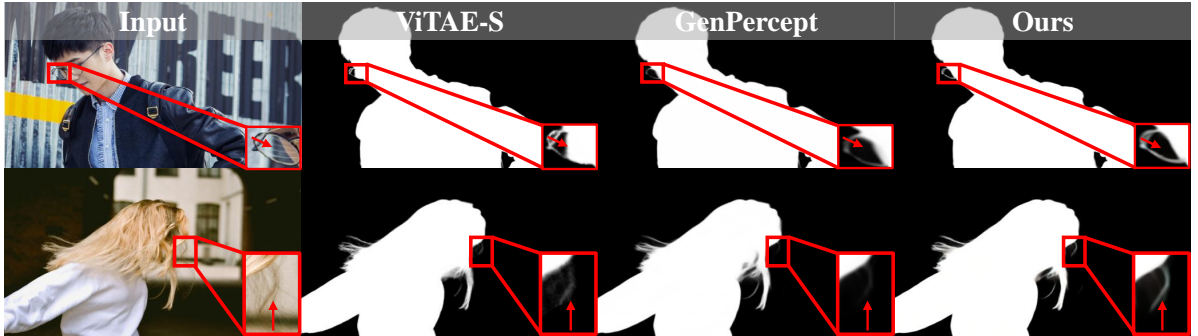


Figure 5. Qualitative comparison of image matting on the P3M-500-NP test set.

the complex structure of the spine, underscoring its excellent fine-grained geometric perception. More comprehensive results on the remaining tasks are in the Appendix.

Table 4. Evaluation of the *Spinal Morphology Assessment* task.

Model	Training Samples	IoU $\uparrow$	PA $\uparrow$	DiCE $\uparrow$	Avg. $\uparrow$
SAM [35]	1.1B	0.555	0.611	0.612	0.593
CLIPSeg [48]	345K	0.519	0.569	0.551	0.546
Grounded-SAM [62]	1.1B	0.464	0.481	0.481	0.475
Ours	15	<b>0.932</b>	<b>0.969</b>	<b>0.963</b>	<b>0.955</b>

### 4.3. Ablation Study

For simplicity, we conduct ablation studies on the representative task of depth estimation. We report results on two standard benchmarks: NYUv2 [69] for indoor scenes and

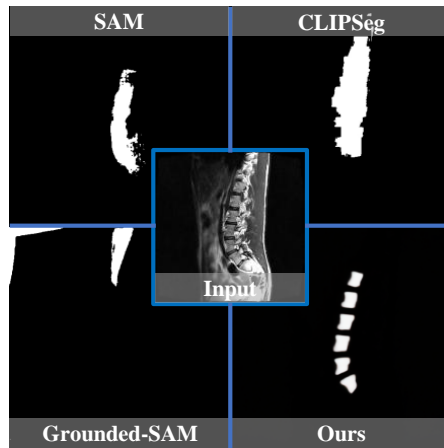


Figure 6. Comparison on the *Spinal Morphology Assessment* task.

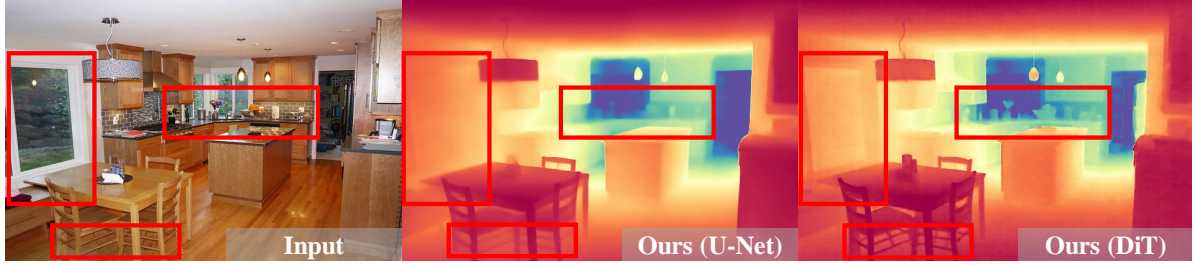


Figure 7. DiT-based D<sup>3</sup>-Predictor exhibits even higher fidelity, indicating that DiT-based architectures hold great potential for further improving diffusion-based dense prediction performance as more computational resources become available.

KITTI [19] for driving scenes.

#### 4.3.1. Training Data Volume

Our method achieves a remarkable balance between training data volume and performance. To further evaluate training data efficiency, we train D<sup>3</sup>-Predictor on varying amounts of synthetic data. As shown in Fig. 8, D<sup>3</sup>-Predictor already delivers acceptable performance even with a limited amount of training data, demonstrating the training data efficiency of our approach. It is worth noting that compared with state-of-the-art discriminative depth estimation models, such as Depth Pro [4], our method exhibits superior data efficiency. First, Depth Pro is trained using a combination of more than twenty heterogeneous datasets, whereas our model only requires a small subset from three datasets. Second, Depth Pro relies on complex data augmentation pipelines to utilize large-scale mixed data, while our method does not require any specialized data processing.

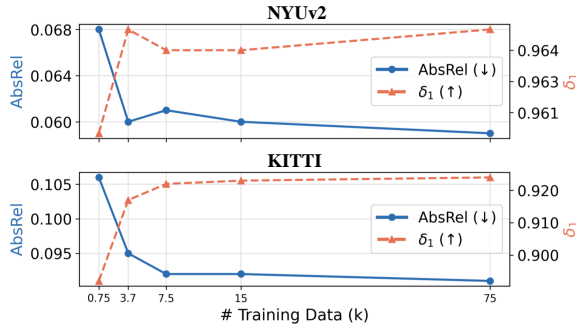


Figure 8. The ablation study on the training data volume.

#### 4.3.2. Improving Generalization with Real Images

As illustrated in Fig. 8, further increasing the amount of synthetic training data to 75K yields only marginal performance gains, suggesting that the limited diversity of synthetic data constrains model generalization. To address this limitation, we train our model on a balanced mixture of synthetic data and real images with pseudo-labels to improve its generalization. This approach is feasible for two main reasons. First, state-of-the-art discriminative models, although less capable of producing fine-grained visual details than diffusion-based methods, typically achieve superior quanti-

tative performance and can generate reliable pseudo-labels for real images. Second, diffusion priors, including our noise-free aggregated diffusion prior, inherently originate from Internet-scale datasets [68], which enables our model to effectively process both synthetic and real data in a unified manner. Table 5 demonstrates that incorporating real images significantly improves the model’s generalization ability across zero-shot real-world benchmarks.

Table 5. Performance comparison of D<sup>3</sup>-Predictor under different training data configurations.

Synthetic + Real	KITTI		NYUv2	
	AbsRel↓	$\delta_1$ ↑	AbsRel↓	$\delta_1$ ↑
7.5K + 7.5K	0.087	0.933	0.060	0.967
15K + 0	0.092	0.923	0.061	0.963
7.5K + 0	0.092	0.922	0.061	0.964

#### 4.3.3. Architecture of Diffusion Model

Recent progress in image generation has shifted from the U-Net architecture to the DiT architecture [56], achieving better image quality and fidelity [37, 38, 77]. We also initialize our D<sup>3</sup>-Predictor with FLUX.1 dev [37], a DiT-based pretrained diffusion model. The detailed design of the DiT-based D<sup>3</sup>-Predictor is provided in the Appendix.

Due to the significant increase in model size (over 15 $\times$ ) and our limited computational resources, we perform only a quick validation on 7.5K synthetic samples using an input resolution of 768 $\times$ 768. Note that this resolution is sub-optimal for FLUX.1 dev [37], which is pretrained on much higher resolutions. As shown in Table 6, the DiT-based D<sup>3</sup>-Predictor achieves competitive quantitative performance compared to the U-Net variant. Furthermore, Fig. 7 reveals that it exhibits higher perceptual fidelity. These findings suggest that the DiT-based D<sup>3</sup>-Predictor holds immense potential for advancing dense prediction performance.

## 5. Conclusion

In this paper, we show that eliminating the stochastic noise inherent in diffusion models is crucial for improving the performance, generalization, and efficiency of

Table 6. Performance comparison of D<sup>3</sup>-Predictor under different diffusion model architectures.

Architecture	KITTI		NYUv2	
	AbsRel $\downarrow$	$\delta_1 \uparrow$	AbsRel $\downarrow$	$\delta_1 \uparrow$
D <sup>3</sup> -Predictor (DiT)	0.095	0.918	0.065	0.959
D <sup>3</sup> -Predictor (U-Net)	0.092	0.922	0.061	0.964

diffusion-based dense prediction. To this end, we propose D<sup>3</sup>-Predictor, a noise-free deterministic diffusion-based dense prediction model that aggregates timestep-dependent priors from the pretrained diffusion model into a complete, noise-free prior in a self-supervised manner. We achieve this by aligning the internal representations of the D<sup>3</sup>-Predictor with those of the pretrained diffusion model. This noise-free aggregated diffusion prior can be effectively leveraged for various dense prediction tasks through simple task-specific supervision. Furthermore, D<sup>3</sup>-Predictor requires less than half the training data previously used, and performs inference in a single step, significantly improving the training efficiency and inference efficiency of diffusion-based dense prediction. Extensive experiments on various dense prediction tasks demonstrate that D<sup>3</sup>-Predictor achieves superior performance and generalization across various dense prediction tasks.

## References

- [1] Gwangbin Bae and Andrew J Davison. Rethinking inductive biases for surface normal estimation. In *Proceedings of the IEEE/CVF Conference on Computer Vision and Pattern Recognition*, pages 9535–9545, 2024. 6
- [2] Yogesh Balaji, Seungjun Nah, Xun Huang, Arash Vahdat, Jiaming Song, Qinsheng Zhang, Karsten Kreis, Miika Aittala, Timo Aila, Samuli Laine, et al. ediff-i: Text-to-image diffusion models with an ensemble of expert denoisers. *arXiv preprint arXiv:2211.01324*, 2022. 2, 3
- [3] Giulio Biroli, Tony Bonnaire, Valentin De Bortoli, and Marc Mézard. Dynamical regimes of diffusion models. *Nature Communications*, 15(1):9957, 2024. 2, 3
- [4] Aleksei Bochkovskii, AmaÃÂgi Delaunoy, Hugo Germain, Marcel Santos, Yichao Zhou, Stephan R Richter, and Vladlen Koltun. Depth pro: Sharp monocular metric depth in less than a second. *arXiv preprint arXiv:2410.02073*, 2024. 2, 5, 8, 3
- [5] Daniel J Butler, Jonas Wulff, Garrett B Stanley, and Michael J Black. A naturalistic open source movie for optical flow evaluation. In *European conference on computer vision*, pages 611–625. Springer, 2012. 5, 2
- [6] Yohann Cabon, Naila Murray, and Martin Humenberger. Virtual kitti 2. *arXiv preprint arXiv:2001.10773*, 2020. 2, 5
- [7] Quan Chen, Tiezheng Ge, Yanyu Xu, Zhiqiang Zhang, Xinxin Yang, and Kun Gai. Semantic human matting. In *Proceedings of the 26th ACM international conference on Multimedia*, pages 618–626, 2018. 6
- [8] Weifeng Chen, Shengyi Qian, David Fan, Noriyuki Kojima, Max Hamilton, and Jia Deng. Oasis: A large-scale dataset for single image 3d in the wild. In *Proceedings of the IEEE/CVF Conference on Computer Vision and Pattern Recognition*, pages 679–688, 2020. 5
- [9] Xi Chen, Sida Peng, Dongchen Yang, Yuan Liu, Bowen Pan, Chengfei Lv, and Xiaowei Zhou. Intrinsicanything: Learning diffusion priors for inverse rendering under unknown illumination. In *European Conference on Computer Vision*, pages 450–467. Springer, 2024. 2
- [10] Ziyi Chen, Xiaolong Wu, and Yu Zhang. Nc-sdf: Enhancing indoor scene reconstruction using neural sdf with view-dependent normal compensation. In *Proceedings of the IEEE/CVF Conference on Computer Vision and Pattern Recognition*, pages 5155–5165, 2024. 2
- [11] Daniel YT Chino, Letricia PS Avalhais, Jose F Rodrigues, and Agma JM Traina. Bowfire: detection of fire in still images by integrating pixel color and texture analysis. In *2015 28th SIBGRAPI conference on graphics, patterns and images*, pages 95–102. IEEE, 2015. 5
- [12] Chengwen Chu, DL Belavy, G Armbrecht, M Bansmann, D Felsenberg, and G Zheng. Annotated t2-weighted mr images of the lower spine. *Zenodo*, 2015. 6, 4
- [13] Angela Dai, Angel X Chang, Manolis Savva, Maciej Halber, Thomas Funkhouser, and Matthias Nießner. Scannet: Richly-annotated 3d reconstructions of indoor scenes. In *Proceedings of the IEEE conference on computer vision and pattern recognition*, pages 5828–5839, 2017. 5
- [14] Ainaz Eftekhari, Alexander Sax, Jitendra Malik, and Amir Zamir. Omnidata: A scalable pipeline for making multi-task mid-level vision datasets from 3d scans. In *Proceedings of the IEEE/CVF International Conference on Computer Vision*, pages 10786–10796, 2021. 6
- [15] Deng-Ping Fan, Ge-Peng Ji, Guolei Sun, Ming-Ming Cheng, Jianbing Shen, and Ling Shao. Camouflaged object detection. In *Proceedings of the IEEE/CVF conference on computer vision and pattern recognition*, pages 2777–2787, 2020. 4
- [16] Rui Fan, Umar Ozgunalp, Brett Hosking, Ming Liu, and Ioannis Pitas. Pothole detection based on disparity transformation and road surface modeling. *IEEE Transactions on Image Processing*, 29:897–908, 2019. 4
- [17] Xiao Fu, Wei Yin, Mu Hu, Kaixuan Wang, Yuexin Ma, Ping Tan, Shaojie Shen, Dahua Lin, and Xiaoxiao Long. Geowizard: Unleashing the diffusion priors for 3d geometry estimation from a single image. In *European Conference on Computer Vision*, pages 241–258. Springer, 2024. 2, 3, 6, 1
- [18] Gonzalo Martin Garcia, Karim Abou Zeid, Christian Schmidt, Daan De Geus, Alexander Hermans, and Bastian Leibe. Fine-tuning image-conditional diffusion models is easier than you think. In *2025 IEEE/CVF Winter Conference on Applications of Computer Vision (WACV)*, pages 753–762. IEEE, 2025. 2, 3, 5, 6
- [19] Andreas Geiger, Philip Lenz, Christoph Stiller, and Raquel Urtasun. Vision meets robotics: The kitti dataset. *The international journal of robotics research*, 32(11):1231–1237, 2013. 5, 8, 3

[20] Clément Godard, Oisin Mac Aodha, Michael Firman, and Gabriel J Brostow. Digging into self-supervised monocular depth estimation. In *Proceedings of the IEEE/CVF international conference on computer vision*, pages 3828–3838, 2019. 2

[21] Ming Gui, Johannes Schusterbauer, Ulrich Prestel, Pingchuan Ma, Dmytro Kotovenko, Olga Grebenkova, Stefan Andreas Baumann, Vincent Tao Hu, and Björn Ommer. Depthfm: Fast generative monocular depth estimation with flow matching. In *Proceedings of the AAAI Conference on Artificial Intelligence*, pages 3203–3211, 2025. 3, 6

[22] Sebastian Haug and Jörn Ostermann. A crop/weed field image dataset for the evaluation of computer vision based precision agriculture tasks. In *Computer Vision - ECCV 2014 Workshops*, pages 105–116, 2015. 5

[23] Jing He, Haodong Li, Wei Yin, Yixun Liang, Leheng Li, Kaiqiang Zhou, Hongbo Zhang, Bingbing Liu, and Ying-Cong Chen. Lotus: Diffusion-based visual foundation model for high-quality dense prediction. *arXiv preprint arXiv:2409.18124*, 2024. 6, 3

[24] Jonathan Ho, Ajay Jain, and Pieter Abbeel. Denoising diffusion probabilistic models. *Advances in neural information processing systems*, 33:6840–6851, 2020. 2

[25] Mu Hu, Wei Yin, Chi Zhang, Zhipeng Cai, Xiaoxiao Long, Hao Chen, Kaixuan Wang, Gang Yu, Chunhua Shen, and Shaojie Shen. Metric3d v2: A versatile monocular geometric foundation model for zero-shot metric depth and surface normal estimation. *IEEE Transactions on Pattern Analysis and Machine Intelligence*, 2024. 2, 5, 6, 3

[26] Shengyu Huang, Zan Gojcic, Zian Wang, Francis Williams, Yoni Kasten, Sanja Fidler, Konrad Schindler, and Or Litany. Neural lidar fields for novel view synthesis. In *Proceedings of the IEEE/CVF International Conference on Computer Vision*, pages 18236–18246, 2023. 4

[27] Immersive Limit. Cigarette butts dataset. <https://www.immersivelimit.com/datasets/cigarette-butts>, 2024. Accessed: 2025-04-30. 5

[28] Dengyang Jiang, Mengmeng Wang, Liuzhuozheng Li, Lei Zhang, Haoyu Wang, Wei Wei, Guang Dai, Yanning Zhang, and Jingdong Wang. No other representation component is needed: Diffusion transformers can provide representation guidance by themselves. *arXiv preprint arXiv:2505.02831*, 2025. 3, 4

[29] Kai Jin, Xingru Huang, Jingxing Zhou, Yunxiang Li, Yan Yan, Yibao Sun, Qianni Zhang, Yaqi Wang, and Juan Ye. Fives: A fundus image dataset for artificial intelligence based vessel segmentation. *Scientific data*, 9(1):475, 2022. 4

[30] Oğuzhan Fatih Kar, Teresa Yeo, Andrei Atanov, and Amir Zamir. 3d common corruptions and data augmentation. In *Proceedings of the IEEE/CVF Conference on Computer Vision and Pattern Recognition*, pages 18963–18974, 2022. 6

[31] Bingxin Ke, Anton Obukhov, Shengyu Huang, Nando Metzger, Rodrigo Caye Daudt, and Konrad Schindler. Repurposing diffusion-based image generators for monocular depth estimation. In *Proceedings of the IEEE/CVF conference on computer vision and pattern recognition*, pages 9492–9502, 2024. 2, 3, 4, 5, 6

[32] Bingxin Ke, Kevin Qu, Tianfu Wang, Nando Metzger, Shengyu Huang, Bo Li, Anton Obukhov, and Konrad Schindler. Marigold: Affordable adaptation of diffusion-based image generators for image analysis. *arXiv preprint arXiv:2505.09358*, 2025. 5, 6, 2, 3

[33] Zhanghan Ke, Jiayu Sun, Kaican Li, Qiong Yan, and Rynson WH Lau. Modnet: Real-time trimap-free portrait matting via objective decomposition. In *Proceedings of the AAAI Conference on Artificial Intelligence*, pages 1140–1147, 2022. 6

[34] killa92. Cardiac semantic segmentation dataset. <https://www.kaggle.com/datasets/killa92/cardiac-semantic-segmentation-dataset>, 2020. Accessed: 2025-04-30. 5

[35] Alexander Kirillov, Eric Mintun, Nikhila Ravi, Hanzi Mao, Chloe Rolland, Laurens Gustafson, Tete Xiao, Samuel Whitehead, Benjamin Caine, Roozbeh Mottaghi, et al. Segment anything. In *Proceedings of the IEEE/CVF Conference on Computer Vision and Pattern Recognition*, pages 21293–21312, 2023. 6, 7, 4, 5

[36] Tobias Koch, Lukas Liebel, Friedrich Fraundorfer, and Marco Körner. Evaluation of cnn-based single-image depth estimation methods. In *Proceedings of the European Conference on Computer Vision (ECCV) Workshops*, pages 0–0, 2018. 5

[37] Black Forest Labs. Flux. <https://github.com/black-forest-labs/flux>, 2024. 8, 2

[38] Black Forest Labs, Stephen Batifol, Andreas Blattmann, Frederic Boesel, Saksham Consul, Cyril Diagne, Tim Dockhorn, Jack English, Zion English, Patrick Esser, Sumith Kulal, Kyle Lacey, Yam Levi, Cheng Li, Dominik Lorenz, Jonas Müller, Dustin Podell, Robin Rombach, Harry Saini, Axel Sauer, and Luke Smith. Flux.1 kontext: Flow matching for in-context image generation and editing in latent space, 2025. 8

[39] Earthshot Labs. Tree binary segmentation. <https://www.kaggle.com/datasets/earthshot/tree-binary-segmentation>, 2022. 4

[40] Duong H Le, Tuan Pham, Sangho Lee, Christopher Clark, Aniruddha Kembhavi, Stephan Mandt, Ranjay Krishna, and Jiasen Lu. One diffusion to generate them all. In *Proceedings of the Computer Vision and Pattern Recognition Conference*, pages 2671–2682, 2025. 5, 6

[41] Hsin-Ying Lee, Hung-Yu Tseng, and Ming-Hsuan Yang. Exploiting diffusion prior for generalizable dense prediction. In *Proceedings of the IEEE/CVF Conference on Computer Vision and Pattern Recognition*, pages 7861–7871, 2024. 2, 6

[42] Gaelle Letort, Adrien Eichmuller, Christelle Da Silva, Elvira Nikalayevich, Flora Crozet, Jeremy Salle, Nicolas Minc, Elsa Labrune, Jean-Philippe Wolf, Marie-Emilie Terret, et al. An interpretable and versatile machine learning approach for oocyte phenotyping. *Journal of Cell Science*, 135(13):jcs260281, 2022. 4, 5

[43] Jizhizi Li, Sihan Ma, Jing Zhang, and Dacheng Tao. Privacy-preserving portrait matting. In *Proceedings of the 29th ACM international conference on multimedia*, pages 3501–3509, 2021. 5, 6

[44] Zhen Li, Mingdeng Cao, Xintao Wang, Zhongang Qi, Ming-Ming Cheng, and Ying Shan. Photomaker: Customizing realistic human photos via stacked id embedding. In *Proceedings of the IEEE/CVF conference on computer vision and pattern recognition*, pages 8640–8650, 2024. 2

[45] Tsung-Yi Lin, Michael Maire, Serge Belongie, James Hays, Pietro Perona, Deva Ramanan, Piotr Dollár, and C Lawrence Zitnick. Microsoft coco: Common objects in context. In *European conference on computer vision*, pages 740–755. Springer, 2014. 5, 2

[46] Ilya Loshchilov and Frank Hutter. Decoupled weight decay regularization. *arXiv preprint arXiv:1711.05101*, 2017. 5

[47] Jiasen Lu, Christopher Clark, Rowan Zellers, Roozbeh Mottaghi, and Aniruddha Kembhavi. Unified-io: A unified model for vision, language, and multi-modal tasks. *arXiv preprint arXiv:2206.08916*, 2022. 6

[48] Theresa Lüddecke and Alexander S Ecker. Image segmentation using text and image prompts. *arXiv preprint arXiv:2112.10003*, 2022. 7, 4, 5

[49] Sihan Ma, Jizhizi Li, Jing Zhang, He Zhang, and Dacheng Tao. Rethinking portrait matting with privacy preserving. *International journal of computer vision*, 131(8):2172–2197, 2023. 6

[50] Yue Ming, Xuyang Meng, Chunxiao Fan, and Hui Yu. Deep learning for monocular depth estimation: A review. *Neurocomputing*, 438:14–33, 2021. 1

[51] David Mizrahi, Roman Bachmann, Oguzhan Kar, Teresa Yeo, Mingfei Gao, Afshin Dehghan, and Amir Zamir. 4m: Massively multimodal masked modeling. *Advances in Neural Information Processing Systems*, 36:58363–58408, 2023. 6

[52] Volodymyr Mnih. *Machine learning for aerial image labeling*. University of Toronto (Canada), 2013. 4, 5

[53] Peter Naylor, Marick Laé, Fabien Reyal, and Thomas Walter. Segmentation of nuclei in histopathology images by deep regression of the distance map. *IEEE transactions on medical imaging*, 38(2):448–459, 2018. 4

[54] Chinese Academy of Cultural Heritage. 2020 sar water body sample and annotation dataset. <https://noda.ac.cn/datassharing/datasetDetails/650427f8671ff33bd4ffedb6>, 2022. Data source for the National Key R&D Program Project "Assessment and Emergency Response for Natural Disaster Risks of Immovable Cultural Heritage" (2019YFC1520800). 4

[55] Maxime Oquab, Timothée Darcet, Théo Moutakanni, Huy Vo, Marc Szafraniec, Vasil Khalidov, Pierre Fernandez, Daniel Haziza, Francisco Massa, Alaaeldin El-Nouby, et al. Dinov2: Learning robust visual features without supervision. *arXiv preprint arXiv:2304.07193*, 2023. 2, 3

[56] William Peebles and Saining Xie. Scalable diffusion models with transformers. In *Proceedings of the IEEE/CVF international conference on computer vision*, pages 4195–4205, 2023. 8

[57] Yu Qiao, Yuhao Liu, Xin Yang, Dongsheng Zhou, Mingliang Xu, Qiang Zhang, and Xiaopeng Wei. Attention-guided hierarchical structure aggregation for image matting. In *Proceedings of the IEEE/CVF Conference on Computer Vision and Pattern Recognition*, pages 13676–13685, 2020. 6

[58] Can Qin, Shu Zhang, Ning Yu, Yihao Feng, Xinyi Yang, Yingbo Zhou, Huan Wang, Juan Carlos Niebles, Caiming Xiong, Silvio Savarese, et al. Unicontrol: A unified diffusion model for controllable visual generation in the wild. *arXiv preprint arXiv:2305.11147*, 2023. 2

[59] Xuebin Qin, Hang Dai, Xiaobin Hu, Deng-Ping Fan, Ling Shao, and Luc Van Gool. Highly accurate dichotomous image segmentation. In *European Conference on Computer Vision*, pages 38–56. Springer, 2022. 5

[60] René Ranftl, Katrin Lasinger, David Hafner, Konrad Schindler, and Vladlen Koltun. Towards robust monocular depth estimation: Mixing datasets for zero-shot cross-dataset transfer. *IEEE transactions on pattern analysis and machine intelligence*, 44(3):1623–1637, 2020. 4, 6, 2

[61] René Ranftl, Alexey Bochkovskiy, and Vladlen Koltun. Vision transformers for dense prediction. In *Proceedings of the IEEE/CVF international conference on computer vision*, pages 12179–12188, 2021. 6

[62] Tianhe Ren, Shilong Liu, Ailing Zeng, Jing Lin, Kunchang Li, He Cao, Jiayu Chen, Xinyu Huang, Yukang Chen, Feng Yan, et al. Grounded sam: Assembling open-world models for diverse visual tasks. *arXiv preprint arXiv:2401.14159*, 2024. 7, 4, 5

[63] Sadjad Rezvani, Mansoor Fateh, and Hossein Khosravi. Abanet: Attention boundary-aware network for image segmentation. *Expert Systems*, 41(9):e13625, 2024. 5

[64] Severi Rissanen, Markus Heinonen, and Arno Solin. Generative modelling with inverse heat dissipation. *arXiv preprint arXiv:2206.13397*, 2022. 3

[65] Mike Roberts, Jason Ramapuram, Anurag Ranjan, Atulit Kumar, Miguel Angel Bautista, Nathan Paczan, Russ Webb, and Joshua M Susskind. Hypersim: A photorealistic synthetic dataset for holistic indoor scene understanding. In *Proceedings of the IEEE/CVF international conference on computer vision*, pages 10912–10922, 2021. 5, 2

[66] Robin Rombach, Andreas Blattmann, Dominik Lorenz, Patrick Esser, and Björn Ommer. High-resolution image synthesis with latent diffusion models. In *Proceedings of the IEEE/CVF conference on computer vision and pattern recognition*, pages 10684–10695, 2022. 2, 5, 1

[67] Thomas Schops, Johannes L Schonberger, Silvano Galliani, Torsten Sattler, Konrad Schindler, Marc Pollefeys, and Andreas Geiger. A multi-view stereo benchmark with high-resolution images and multi-camera videos. In *Proceedings of the IEEE conference on computer vision and pattern recognition*, pages 3260–3269, 2017. 5

[68] Christoph Schuhmann, Romain Beaumont, Richard Vencu, Cade Gordon, Ross Wightman, Mehdi Cherti, Theo Coombes, Aarush Katta, Clayton Mullis, Mitchell Wortsman, et al. Laion-5b: An open large-scale dataset for training next generation image-text models. *Advances in neural information processing systems*, 35:25278–25294, 2022. 8

[69] Nathan Silberman, Derek Hoiem, Pushmeet Kohli, and Rob Fergus. Indoor segmentation and support inference from rgbd images. In *European conference on computer vision*, pages 746–760. Springer, 2012. 5, 7, 3

[70] Nick Stracke, Stefan Andreas Baumann, Kolja Bauer, Frank Fundel, and Björn Ommer. Cleandift: Diffusion features

without noise. In *Proceedings of the Computer Vision and Pattern Recognition Conference*, pages 117–127, 2025. 2, 3, 4

[71] Luming Tang, Menglin Jia, Qianqian Wang, Cheng Perng Phoo, and Bharath Hariharan. Emergent correspondence from image diffusion. *Advances in Neural Information Processing Systems*, 36:1363–1389, 2023. 3

[72] Narek Tumanyan, Michal Geyer, Shai Bagon, and Tali Dekel. Plug-and-play diffusion features for text-driven image-to-image translation. In *Proceedings of the IEEE/CVF conference on computer vision and pattern recognition*, pages 1921–1930, 2023. 1

[73] Igor Vasiljevic, Nick Kolkin, Shanyi Zhang, Ruotian Luo, Haochen Wang, Falcon Z Dai, Andrea F Daniele, Mohammadreza Mostajabi, Steven Basart, Matthew R Walter, et al. Diode: A dense indoor and outdoor depth dataset. *corr abs/1908.00463* (2019), 1908. 5

[74] Liming Wang, Jianbo Shi, Gang Song, and I-fan Shen. Object detection combining recognition and segmentation. In *Asian conference on computer vision*, pages 189–199. Springer, 2007. 4

[75] Wen Wang, Qiuyu Wang, Kecheng Zheng, Hao Ouyang, Zhehai Chen, Biao Gong, Hao Chen, Yujun Shen, and Chunhua Shen. Framer: Interactive frame interpolation. *arXiv preprint arXiv:2410.18978*, 2024. 2

[76] Xiaolong Wang, David Fouhey, and Abhinav Gupta. Designing deep networks for surface normal estimation. In *Proceedings of the IEEE conference on computer vision and pattern recognition*, pages 539–547, 2015. 1

[77] Chenfei Wu, Jiahao Li, Jingren Zhou, Junyang Lin, Kaiyuan Gao, Kun Yan, Sheng-ming Yin, Shuai Bai, Xiao Xu, Yile Chen, et al. Qwen-image technical report. *arXiv preprint arXiv:2508.02324*, 2025. 8

[78] Ge Wu, Shen Zhang, Ruijing Shi, Shanghua Gao, Zhenyuan Chen, Lei Wang, Zhaowei Chen, Hongcheng Gao, Yao Tang, Jian Yang, et al. Representation entanglement for generation: Training diffusion transformers is much easier than you think. *arXiv preprint arXiv:2507.01467*, 2025. 3, 4, 2

[79] Guangkai Xu, Yongtao Ge, Mingyu Liu, Chengxiang Fan, Kangyang Xie, Zhiyue Zhao, Hao Chen, and Chunhua Shen. Diffusion models trained with large data are transferable visual models. *CoRR*, 2024. 2

[80] Guangkai Xu, Yongtao Ge, Mingyu Liu, Chengxiang Fan, Kangyang Xie, Zhiyue Zhao, Hao Chen, and Chunhua Shen. What matters when repurposing diffusion models for general dense perception tasks? *arXiv preprint arXiv:2403.06090*, 2024. 2, 3, 4, 5, 6

[81] Lihe Yang, Bingyi Kang, Zilong Huang, Xiaogang Xu, Jiashi Feng, and Hengshuang Zhao. Depth anything: Unleashing the power of large-scale unlabeled data. In *Proceedings of the IEEE/CVF conference on computer vision and pattern recognition*, pages 10371–10381, 2024. 6

[82] Lihe Yang, Bingyi Kang, Zilong Huang, Zhen Zhao, Xiaogang Xu, Jiashi Feng, and Hengshuang Zhao. Depth anything v2. *Advances in Neural Information Processing Systems*, 37:21875–21911, 2024. 6

[83] Zhuoyi Yang, Jiayan Teng, Wendi Zheng, Ming Ding, Shiyu Huang, Jiazheng Xu, Yuanming Yang, Wenyi Hong, Xiaohan Zhang, Guanyu Feng, et al. Cogvideox: Text-to-video diffusion models with an expert transformer. *arXiv preprint arXiv:2408.06072*, 2024. 2

[84] Chongjie Ye, Lingteng Qiu, Xiaodong Gu, Qi Zuo, Yushuang Wu, Zilong Dong, Liefeng Bo, Yuliang Xiu, and Xiaoguang Han. Stablenormal: Reducing diffusion variance for stable and sharp normal. *ACM Transactions on Graphics (TOG)*, 43(6):1–18, 2024. 2, 3, 6

[85] Wei Yin, Xinlong Wang, Chunhua Shen, Yifan Liu, Zhi Tian, Songcen Xu, Changming Sun, and Dou Renyin. Diversedepth: Affine-invariant depth prediction using diverse data. *arXiv preprint arXiv:2002.00569*, 2020. 6

[86] Sihyun Yu, Sangkyung Kwak, Huiwon Jang, Jongheon Jeong, Jonathan Huang, Jinwoo Shin, and Saining Xie. Representation alignment for generation: Training diffusion transformers is easier than you think. *arXiv preprint arXiv:2410.06940*, 2024. 3, 4, 2

[87] Zheng Zeng, Valentin Deschaintre, Iliyan Georgiev, Yannick Hold-Geoffroy, Yiwei Hu, Fujun Luan, Ling-Qi Yan, and Miloš Hašan. Rgb↔x: Image decomposition and synthesis using material- and lighting-aware diffusion models. In *ACM SIGGRAPH 2024 Conference Proceedings*, 2024. 2

[88] Chi Zhang, Wei Yin, Billb Wang, Gang Yu, Bin Fu, and Chunhua Shen. Hierarchical normalization for robust monocular depth estimation. *Advances in Neural Information Processing Systems*, 35:14128–14139, 2022. 6

[89] Lei Zhang, Fan Yang, Yimin Daniel Zhang, and Ying Julie Zhu. Road crack detection using deep convolutional neural network. In *2016 IEEE international conference on image processing (ICIP)*, pages 3708–3712. IEEE, 2016. 4

[90] Wenyuan Zhang, Yixiao Yang, Han Huang, Liang Han, Kanle Shi, Yu-Shen Liu, and Zhizhong Han. Monoinstance: Enhancing monocular priors via multi-view instance alignment for neural rendering and reconstruction. In *Proceedings of the Computer Vision and Pattern Recognition Conference*, pages 21642–21653, 2025. 2

[91] Canyu Zhao, Mingyu Liu, Wen Wang, Weihua Chen, Fan Wang, Hao Chen, Bo Zhang, and Chunhua Shen. Moviedreamer: Hierarchical generation for coherent long visual sequence. *arXiv preprint arXiv:2407.16655*, 2024. 2

[92] Canyu Zhao, Yanlong Sun, Mingyu Liu, Huanyi Zheng, Muzhi Zhu, Zhiyue Zhao, Hao Chen, Tong He, and Chunhua Shen. Dception: A generalist diffusion model for visual perceptual tasks. *arXiv preprint arXiv:2502.17157*, 2025. 2, 3, 4, 6

[93] Qiqi Zhu, Yanan Zhang, Ziqi Li, Xiaorui Yan, Qingfeng Guan, Yanfei Zhong, Liangpei Zhang, and Deren Li. Oil spill contextual and boundary-supervised detection network based on marine sar images. *IEEE Transactions on Geoscience and Remote Sensing*, 60:1–10, 2021. 4

# D<sup>3</sup>-Predictor: Noise-Free Deterministic Diffusion for Dense Prediction

## Supplementary Material

This supplementary material provides additional details and more qualitative and quantitative analysis to complement the main paper. The content is organized as follows:

- More Implementation Details (Appendix 6)
- Additional Visualization Results (Appendix 7)
- Additional Experimental Results (Appendix 8)

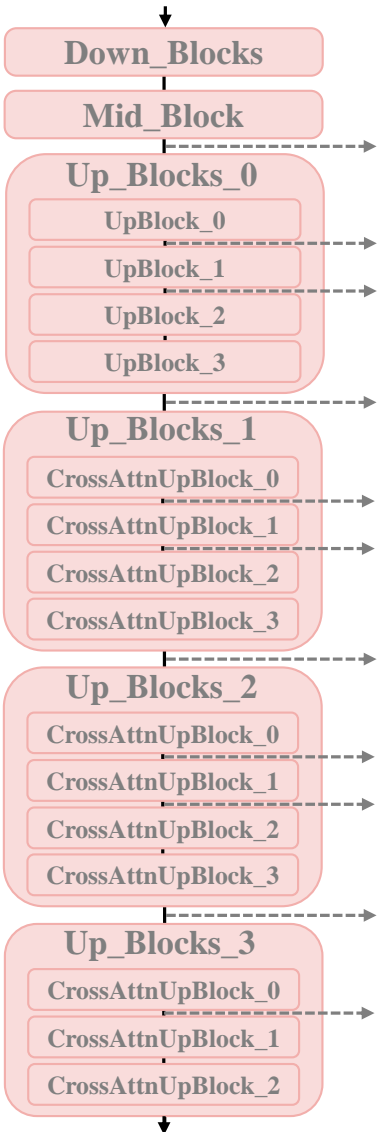


Figure 9. We carefully selected the internal representations from the U-Net-based D<sup>3</sup>-Predictor for self-supervised alignment.

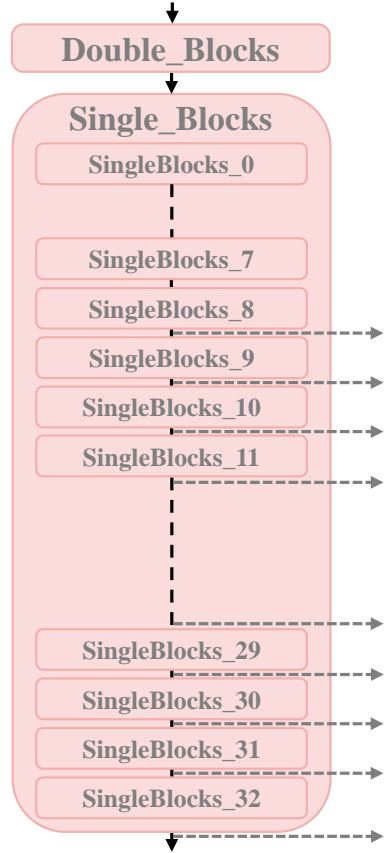


Figure 10. We carefully selected the internal representations from the DiT-based D<sup>3</sup>-Predictor for self-supervised alignment.

## 6. More Implementation Details

### 6.1. Model Architecture

#### 6.1.1. U-Net-Based D<sup>3</sup>-Predictor

The U-Net-based D<sup>3</sup>-Predictor is initialized using the pre-trained Stable Diffusion v2.1 (SD v2.1) [66]. Figure 9 illustrates the backbone architecture of SD v2.1 and highlights the specific internal representations selected for self-supervised alignment (indicated by dashed arrows).

The selection of layers for representation alignment is critical. Prior work [72] suggests that SD's upsampling blocks encode rich spatial semantic information that is largely invariant to appearance features (e.g., style and texture), focusing instead on underlying structure and shape. Inspired by this finding, we hypothesize that the internal representations from SD's upsampling blocks are optimally suited for dense prediction, given that this task is fundamentally an image-to-structure mapping [17]. To maintain effi-

ciency without compromising alignment quality, we carefully chose a minimal set of layers. This selection captures sufficient multi-scale structural detail while avoiding the high computational cost of aligning redundant representations. Consequently, we select the specific internal representations indicated by the dashed arrows in Figure 9.

### 6.1.2. DiT-Based D<sup>3</sup>-Predictor

The DiT-based D<sup>3</sup>-Predictor is initialized using the pre-trained FLUX.1 dev model [37]. Figure 10 presents the backbone architecture of FLUX.1 dev and indicates the internal representations selected for the self-supervised alignment (marked by dashed arrows). Drawing upon the insights from the U-Net-based D<sup>3</sup>-Predictor implementation, we focus on the representations from the deeper layers which typically carry refined spatial and structural information in DiT architectures. Specifically, we select the representations from the last 25 single-flow blocks for robust and effective representation alignment.

## 6.2. Text Prompt

Text prompts provide diverse guidance for creative image [44, 58, 79] and video [75, 83, 91] generation, ensuring the results align with user intent. Despite their utility in creative tasks, extensive prior works [31, 32, 80, 92] suggest that complex text prompts are unnecessary for diffusion-based dense prediction models. This is primarily because dense prediction is a deterministic mapping from image to geometric structure [17], which does not require textual guidance for diversity. Consequently, the D<sup>3</sup>-Predictor utilizes a simple, fixed text prompt for each task to efficiently maintain the necessary context:

Text prompt for depth estimation

A grayscale depth estimation image, where darker areas represent closer depths and lighter areas indicate farther depths.

Text prompt for surface normal estimation

A surface normal estimation map.

Text prompt for image matting

A human portrait matting map.

## 6.3. Training Datasets Mixing Strategy

As described in Section 4.1.1 of our main paper, we utilize multiple training datasets for both depth and surface normal estimation. Inspired by previous work [17, 18], we implement the following dataset sampling configuration in each iteration: For depth estimation, we sample Hypersim

[65] at a rate of 0.76, Virtual KITTI [6] at 0.12, and COCO [45] with pseudo-depth labels generated by Depth Pro [4] at 0.12; for surface normal estimation, we sample Hyper-sim [65] at a rate of 0.9 and Sintel [5] at 0.1.

## 6.4. Training Objective

As described in Section 3.2 of our main paper, the training objective of the D<sup>3</sup>-Predictor is composed of two components that are jointly optimized.

The first part of the objective is the *Self-Supervised Diffusion Priors Aggregation*, which is implemented via the alignment of internal representations. Given that prior works [78, 86] have demonstrated the established efficacy of negative cosine similarity for representation alignment in diffusion models, we adopt it as the alignment metric  $\text{dist}(\cdot, \cdot)$  in Equation 2.

The second part of the objective is the *Task-Specific Supervision*. We achieve this by minimizing the task-specific loss  $\mathcal{L}_{\text{task}}$ , which applies explicit supervision to the model’s final prediction.

For depth estimation,  $\mathcal{L}_{\text{task}}$  is formulated as a weighted combination of three components: the MSE loss  $\mathcal{L}_{\text{MSE}}$ , the affine-invariant loss  $\mathcal{L}_{\text{aff}}$  [60], and the gradient loss in log space  $\mathcal{L}_{\text{grad}}$  [60]. Specifically,  $\mathcal{L}_{\text{task}}$  is defined as:

$$\mathcal{L}_{\text{task}} = \lambda_{\text{MSE}} \cdot \mathcal{L}_{\text{MSE}} + \lambda_{\text{aff}} \cdot \mathcal{L}_{\text{aff}} + \lambda_{\text{grad}} \cdot \mathcal{L}_{\text{grad}} \quad (4)$$

where the weighting coefficients are set to  $\lambda_{\text{MSE}} = 8.0$ ,  $\lambda_{\text{aff}} = 2.0$ , and  $\lambda_{\text{grad}} = 100.0$ .

For surface normal estimation,  $\mathcal{L}_{\text{task}}$  is defined as a weighted sum of the MSE loss  $\mathcal{L}_{\text{MSE}}$  and the angular loss  $\mathcal{L}_{\text{ang}}$ . Specifically,  $\mathcal{L}_{\text{task}}$  is formulated as:

$$\mathcal{L}_{\text{task}} = \lambda_{\text{MSE}} \cdot \mathcal{L}_{\text{MSE}} + \lambda_{\text{ang}} \cdot \mathcal{L}_{\text{ang}} \quad (5)$$

where the weighting coefficients are set to  $\lambda_{\text{MSE}} = 8.0$  and  $\lambda_{\text{ang}} = 3.0$ .

For image matting,  $\mathcal{L}_{\text{task}}$  is defined as a weighted sum of the MSE loss  $\mathcal{L}_{\text{MSE}}$ , the  $\mathcal{L}_1$  loss  $\mathcal{L}_1$ , and the gradient loss  $\mathcal{L}_{\text{grad}}$ . Specifically,  $\mathcal{L}_{\text{task}}$  is formulated as:

$$\mathcal{L}_{\text{task}} = \lambda_{\text{MSE}} \cdot \mathcal{L}_{\text{MSE}} + \lambda_1 \cdot \mathcal{L}_1 + \lambda_{\text{grad}} \cdot \mathcal{L}_{\text{grad}} \quad (6)$$

where the weighting coefficients are set to  $\lambda_{\text{MSE}} = 5.0$ ,  $\lambda_1 = 10.0$ , and  $\lambda_{\text{grad}} = 50.0$ .

## 7. Additional Visualization Results

We provide additional visualization results in Figures 11 through 14, encompassing a diverse range of scenarios such as real-world scenes, AIGC (AI-Generated Content) scenes, and domain-specific scenes. These comprehensive visualizations further demonstrate the D<sup>3</sup>-Predictor’s outstanding ability to generate fine geometric details, its strong generalization capability, and its practical utility.

## 8. Additional Experimental Results

### 8.1. Ablation on Projection Head

We conduct an ablation study to investigate the contribution of the timestep-conditioned projection head used to map the internal representations of the D<sup>3</sup>-Predictor. We evaluate the performance of the D<sup>3</sup>-Predictor when trained with and without the projection head. Following the setup detailed in Section 4.3 of our main paper, we report results on two standard depth estimation benchmarks: NYUv2 [69] for indoor scenes and KITTI [19] for driving scenes. The comparison results, shown in Table 7, consistently demonstrate that the D<sup>3</sup>-Predictor trained with the projection head outperforms the model trained without it on both benchmarks. This indicates that the projection head is essential for effectively bridging the representation of the D<sup>3</sup>-Predictor and the timestep-dependent representations extracted from the pretrained diffusion model.

Table 7. Ablation study on the projection head. Other training settings are the same as our main experiments.

Projection Head	KITTI		NYUv2	
	AbsRel $\downarrow$	$\delta_1 \uparrow$	AbsRel $\downarrow$	$\delta_1 \uparrow$
Yes	0.082	0.940	0.052	0.970
No	0.089	0.930	0.057	0.964

### 8.2. Necessity of Synthetic Training Data

In our main experiments, the optimal performance of the D<sup>3</sup>-Predictor is achieved by training with a mix of synthetic data and pseudo-labeled real data. During training, synthetic data provides high-quality geometric details, while real data contributes to diverse-scene generalization. Section 4.3.2 empirically demonstrates the generalization benefits introduced by real images. Meanwhile, we argue that high-quality synthetic data is also indispensable for strong model performance, as evidenced by the results in Table 8.

Table 8. Performance comparison of D<sup>3</sup>-Predictor under different training data configurations.

Synthetic + Real	KITTI		NYUv2	
	AbsRel $\downarrow$	$\delta_1 \uparrow$	AbsRel $\downarrow$	$\delta_1 \uparrow$
7.5K + 7.5K	0.087	0.933	0.060	0.967
15K + 0	0.092	0.923	0.061	0.963
0 + 15K	0.089	0.928	0.061	0.960

### 8.3. Efficiency and Runtime Analysis

We conduct a thorough analysis of the efficiency of the D<sup>3</sup>-Predictor, summarizing the results in Table 9. The reported inference time is the average runtime over 5,000 images at 768  $\times$  768 resolution on a single NVIDIA L40S

GPU. Our D<sup>3</sup>-Predictor achieves the fastest inference speed among all evaluated baselines. Specifically, our method is approximately 66% faster than the discriminative model Metric3Dv2 [25] and achieves nearly a 10% speedup over the fastest comparable diffusion-based methods, such as E2E-FT [18] and Lotus-G [23].

Beyond speed, the D<sup>3</sup>-Predictor demonstrates highly competitive GPU memory efficiency. While Lotus-G [23] maintains the minimum memory consumption, our model’s usage is comparable and represents a significant saving of nearly 50% compared to the most memory-intensive baseline, Depth Pro [4]. Even when compared to other efficient diffusion-based models like E2E-FT [18], we still achieve over 20% savings in memory consumption. This excellent performance in both inference time and memory requirement confirms that the D<sup>3</sup>-Predictor is an efficiency diffusion-based method while maintaining high predictive performance.

Table 9. Efficiency and runtime analysis. We compare D<sup>3</sup>-Predictor with two leading discriminative models and selected diffusion models operating in  $NFEs=1$  mode. Diffusion-based methods that require ensemble procedures or multi-step inference are excluded due to their significantly higher computational costs.

Method	Time (s)	Memory (GB)
<i>Discriminative Models</i>		
Metric3Dv2 [25]	$\sim 0.66$	7.5
Depth Pro [4]	$\sim 0.64$	12.2
<i>Diffusion Models (NFEs=1)</i>		
E2E-FT [18]	$\sim 0.27$	8.07
Marigold-Normals [32]	$\sim 0.45$	8.04
Lotus-G [23]	$\sim 0.25$	5.72
GenPercept [80]	$\sim 0.28$	8.05
Ours	$\sim 0.22$	6.38

### 8.4. Generalization to Domain-Specific Tasks

Section 4.2.4 of our main paper further evaluates the generalization capability and practical utility of the D<sup>3</sup>-Predictor across 20 additional domain-specific dense prediction tasks. These tasks cover a wide range of practical application fields, including healthcare, ecological monitoring, public safety, and infrastructure inspection. A comprehensive overview of the results on these 20 tasks is presented in Tables 10 through 29. Our model significantly outperforms all zero-shot baselines across all 20 tasks, demonstrating strong zero-shot generalization and establishing a robust foundation model for numerous practical downstream applications.

Table 10. Evaluation of the *Pavement Crack Detect* task [89].

Model	Training Samples	IoU $\uparrow$	PA $\uparrow$	DiCE $\uparrow$
SAM [35]	1.1B	0.351	0.453	0.400
CLIPSeg [48]	345K	<u>0.487</u>	<u>0.499</u>	<u>0.493</u>
Grounded-SAM [62]	1.1B	0.393	0.429	0.428
Ours	15	<b>0.694</b>	<b>0.730</b>	<b>0.766</b>

Table 11. Evaluation of the *Auto. Pothole Detect* task [16].

Model	Training Samples	IoU $\uparrow$	PA $\uparrow$	DiCE $\uparrow$
SAM [35]	1.1B	0.162	0.415	0.186
CLIPSeg [48]	345K	<u>0.597</u>	<u>0.819</u>	<u>0.668</u>
Grounded-SAM [62]	1.1B	0.429	0.469	0.460
Ours	15	<b>0.793</b>	<b>0.828</b>	<b>0.839</b>

Table 12. Evaluation of the *Pedestrian Safety Monitor* task [74].

Model	Training Samples	IoU $\uparrow$	PA $\uparrow$	DiCE $\uparrow$
SAM [35]	1.1B	0.417	0.495	0.478
CLIPSeg [48]	345K	<u>0.616</u>	<u>0.717</u>	<u>0.687</u>
Grounded-SAM [62]	1.1B	0.423	0.505	0.478
Ours	15	<b>0.878</b>	<b>0.939</b>	<b>0.929</b>

Table 13. Evaluation of the *Precise Road Model* task [52].

Model	Training Samples	IoU $\uparrow$	PA $\uparrow$	DiCE $\uparrow$
SAM [35]	1.1B	0.434	0.465	0.464
CLIPSeg [48]	345K	<u>0.439</u>	<u>0.562</u>	<u>0.505</u>
Grounded-SAM [62]	1.1B	0.278	0.472	0.357
Ours	15	<b>0.646</b>	<b>0.711</b>	<b>0.731</b>

Table 14. Evaluation of the *Retinal Vessel Analysis* task [29].

Model	Training Samples	IoU $\uparrow$	PA $\uparrow$	DiCE $\uparrow$
SAM [35]	1.1B	0.273	<u>0.594</u>	0.370
CLIPSeg [48]	345K	<u>0.472</u>	0.510	<u>0.499</u>
Grounded-SAM [62]	1.1B	0.344	0.376	0.409
Ours	15	<b>0.757</b>	<b>0.789</b>	<b>0.837</b>

Table 15. Evaluation of the *Spinal Morphology Assessment* task [12].

Model	Training Samples	IoU $\uparrow$	PA $\uparrow$	DiCE $\uparrow$
SAM [35]	1.1B	<u>0.555</u>	<u>0.611</u>	<u>0.612</u>
CLIPSeg [48]	345K	0.519	0.569	0.551
Grounded-SAM [62]	1.1B	0.464	0.481	0.481
Ours	15	<b>0.932</b>	<b>0.969</b>	<b>0.963</b>

Table 16. Evaluation of the *Oocyte Detect* task [42].

Model	Training Samples	IoU $\uparrow$	PA $\uparrow$	DiCE $\uparrow$
SAM [35]	1.1B	<u>0.952</u>	<u>0.974</u>	<u>0.969</u>
CLIPSeg [48]	345K	0.366	0.500	0.422
Grounded-SAM [62]	1.1B	0.390	0.518	0.460
Ours	15	<b>0.981</b>	<b>0.991</b>	<b>0.990</b>

Table 17. Evaluation of the *Nucleus Localization* task [53].

Model	Training Samples	IoU $\uparrow$	PA $\uparrow$	DiCE $\uparrow$
SAM [35]	1.1B	0.277	0.498	0.336
CLIPSeg [48]	345K	<u>0.452</u>	<u>0.511</u>	0.488
Grounded-SAM [62]	1.1B	0.447	0.506	0.496
Ours	15	<b>0.814</b>	<b>0.880</b>	<b>0.884</b>

Table 18. Evaluation of the *Water Body Map* task [54].

Model	Training Samples	IoU $\uparrow$	PA $\uparrow$	DiCE $\uparrow$
SAM [35]	1.1B	0.299	0.415	0.348
CLIPSeg [48]	345K	0.172	<u>0.504</u>	0.235
Grounded-SAM [62]	1.1B	<u>0.322</u>	0.435	<u>0.406</u>
Ours	15	<b>0.690</b>	<b>0.863</b>	<b>0.754</b>

Table 19. Evaluation of the *Auto. Tree Tagging* task [39].

Model	Training Samples	IoU $\uparrow$	PA $\uparrow$	DiCE $\uparrow$
SAM [35]	1.1B	<u>0.765</u>	<u>0.840</u>	<u>0.809</u>
CLIPSeg [48]	345K	0.463	0.722	0.579
Grounded-SAM [62]	1.1B	0.391	0.529	0.457
Ours	15	<b>0.857</b>	<b>0.931</b>	<b>0.898</b>

Table 20. Evaluation of the *Camouflage Detect* task [15].

Model	Training Samples	IoU $\uparrow$	PA $\uparrow$	DiCE $\uparrow$
SAM [35]	1.1B	0.548	0.612	0.601
CLIPSeg [48]	345K	<u>0.569</u>	<u>0.753</u>	<u>0.667</u>
Grounded-SAM [62]	1.1B	0.454	0.504	0.497
Ours	15	<b>0.714</b>	<b>0.784</b>	<b>0.770</b>

Table 21. Evaluation of the *Oil Spill Track* task [93].

Model	Training Samples	IoU $\uparrow$	PA $\uparrow$	DiCE $\uparrow$
SAM [35]	1.1B	0.133	0.437	0.187
CLIPSeg [48]	345K	<u>0.427</u>	<u>0.618</u>	<u>0.511</u>
Grounded-SAM [62]	1.1B	0.376	0.490	0.463
Ours	15	<b>0.761</b>	<b>0.860</b>	<b>0.839</b>

Table 22. Evaluation of the *Urban Layout Analysis* task [52].

Model	Training Samples	IoU $\uparrow$	PA $\uparrow$	DiCE $\uparrow$
SAM [35]	1.1B	<u>0.386</u>	0.475	<u>0.437</u>
CLIPSeg [48]	345K	0.315	<u>0.616</u>	0.421
Grounded-SAM [62]	1.1B	0.284	0.555	0.390
Ours	15	<b>0.653</b>	<b>0.741</b>	<b>0.756</b>

Table 23. Evaluation of the *Weed Distribution Mapping* task [22].

Model	Training Samples	IoU $\uparrow$	PA $\uparrow$	DiCE $\uparrow$
SAM [35]	1.1B	0.364	0.399	0.398
CLIPSeg [48]	345K	<u>0.609</u>	<u>0.858</u>	<u>0.725</u>
Grounded-SAM [62]	1.1B	0.126	0.420	0.173
Ours	15	<b>0.924</b>	<b>0.952</b>	<b>0.959</b>

Table 24. Evaluation of the *Mask-Wear Monitor* task [63].

Model	Training Samples	IoU $\uparrow$	PA $\uparrow$	DiCE $\uparrow$
SAM [35]	1.1B	<u>0.540</u>	<u>0.614</u>	0.584
CLIPSeg [48]	345K	0.377	0.513	0.469
Grounded-SAM [62]	1.1B	0.377	0.498	0.405
Ours	15	<b>0.903</b>	<b>0.943</b>	<b>0.942</b>

Table 25. Evaluation of the *Cigarette Detect* task [27].

Model	Training Samples	IoU $\uparrow$	PA $\uparrow$	DiCE $\uparrow$
SAM [35]	1.1B	0.304	0.308	0.324
CLIPSeg [48]	345K	<u>0.495</u>	<u>0.500</u>	<u>0.497</u>
Grounded-SAM [62]	1.1B	0.479	0.483	0.486
Ours	15	<b>0.875</b>	<b>0.908</b>	<b>0.904</b>

Table 26. Evaluation of the *Fire Alert* task [11].

Model	Training Samples	IoU $\uparrow$	PA $\uparrow$	DiCE $\uparrow$
SAM [35]	1.1B	0.528	0.591	0.574
CLIPSeg [48]	345K	<u>0.642</u>	<u>0.753</u>	<u>0.710</u>
Grounded-SAM [62]	1.1B	0.469	0.530	0.516
Ours	15	<b>0.829</b>	<b>0.951</b>	<b>0.889</b>

Table 27. Evaluation of the *Food Cell Inspect* task [42].

Model	Training Samples	IoU $\uparrow$	PA $\uparrow$	DiCE $\uparrow$
SAM [35]	1.1B	<u>0.936</u>	<u>0.961</u>	0.959
CLIPSeg [48]	345K	0.291	0.500	0.367
Grounded-SAM [62]	1.1B	0.402	0.561	0.487
Ours	15	<b>0.976</b>	<b>0.988</b>	<b>0.987</b>

Table 28. Evaluation of the *Close-Range Segment* task [59].

Model	Training Samples	IoU $\uparrow$	PA $\uparrow$	DiCE $\uparrow$
SAM [35]	1.1B	0.412	0.478	0.474
CLIPSeg [48]	345K	0.429	0.498	0.459
Grounded-SAM [62]	1.1B	<u>0.436</u>	<u>0.566</u>	<u>0.516</u>
Ours	15	<b>0.655</b>	<b>0.734</b>	<b>0.731</b>

Table 29. Evaluation of the *Cardiac Screen* task [34].

Model	Training Samples	IoU $\uparrow$	PA $\uparrow$	DiCE $\uparrow$
SAM [35]	1.1B	<u>0.535</u>	<u>0.611</u>	<u>0.612</u>
CLIPSeg [48]	345K	0.519	0.569	0.551
Grounded-SAM [62]	1.1B	0.464	0.481	0.481
Ours	15	<b>0.885</b>	<b>0.959</b>	<b>0.935</b>

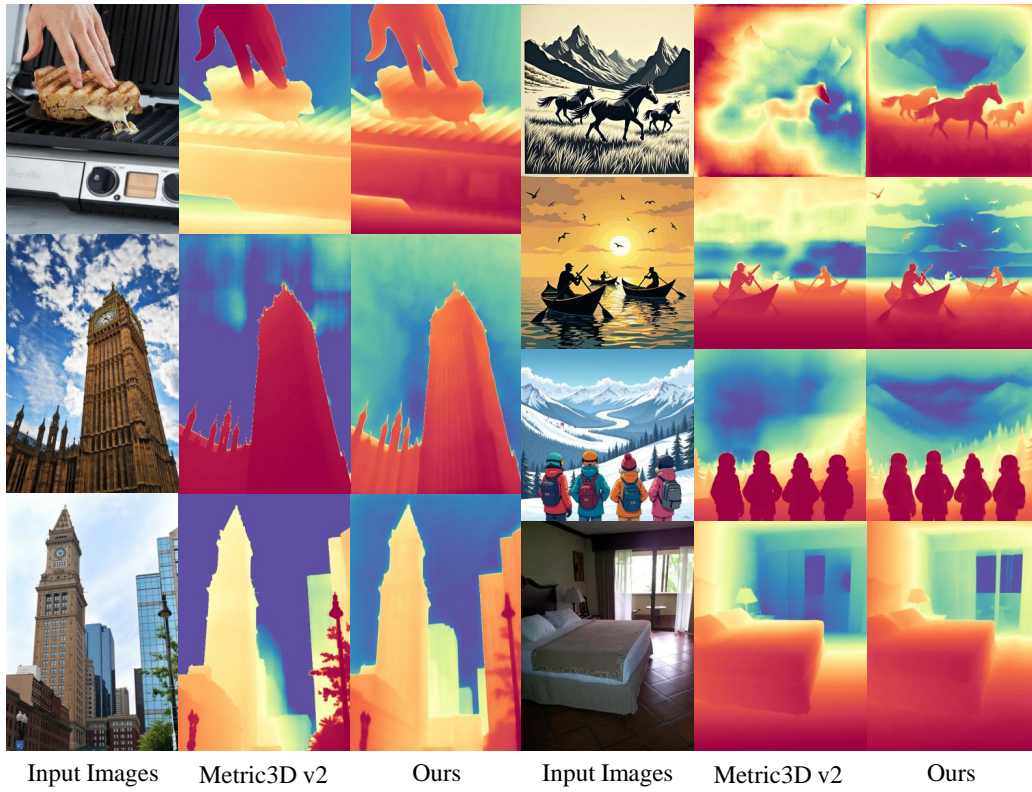


Figure 11. More visualization results for the depth estimation task.



Figure 12. More visualization results for the surface normal estimation task.

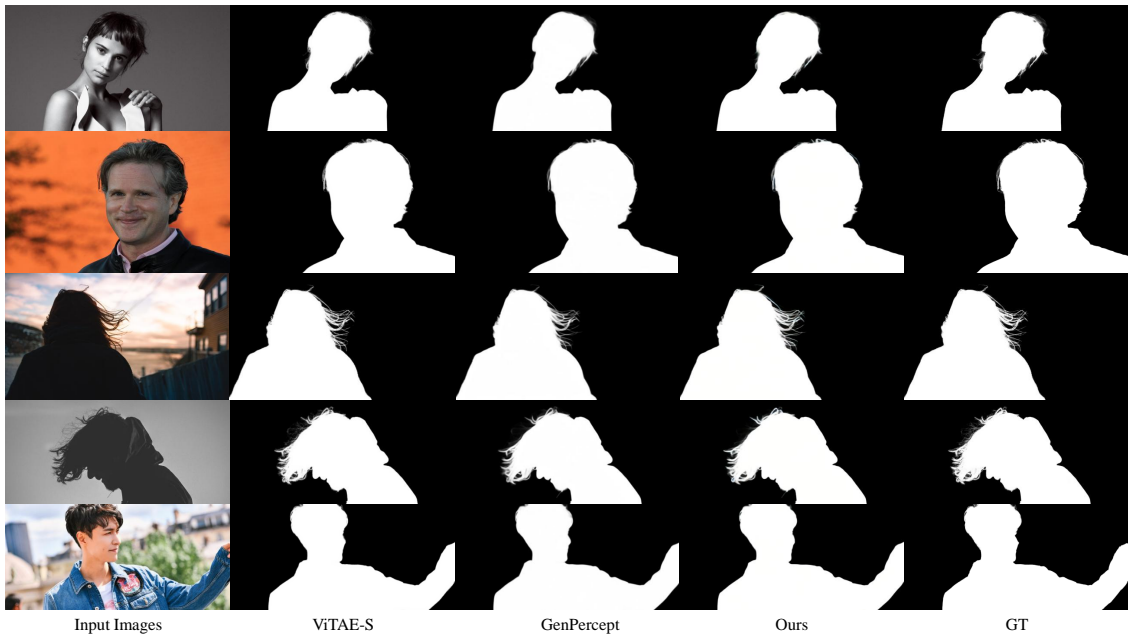
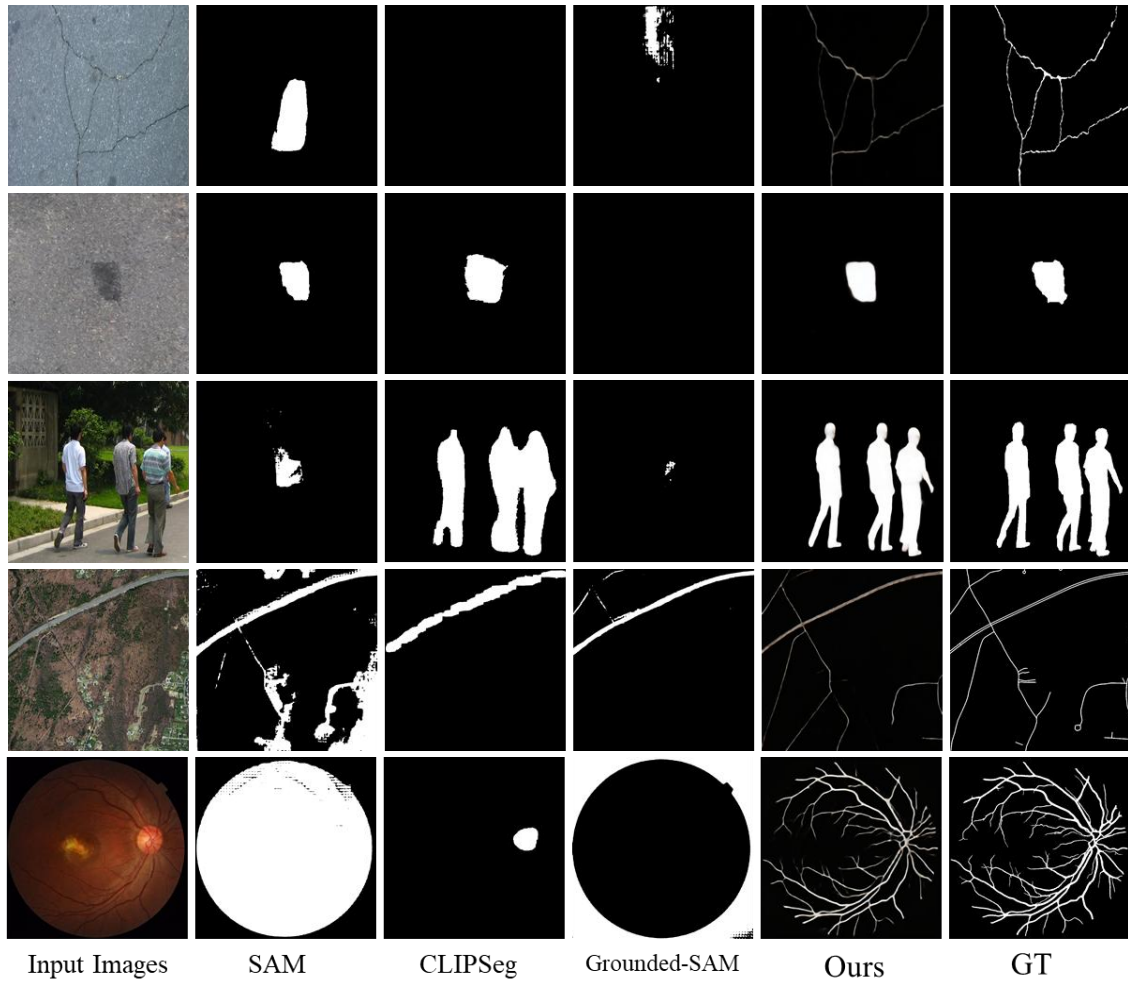
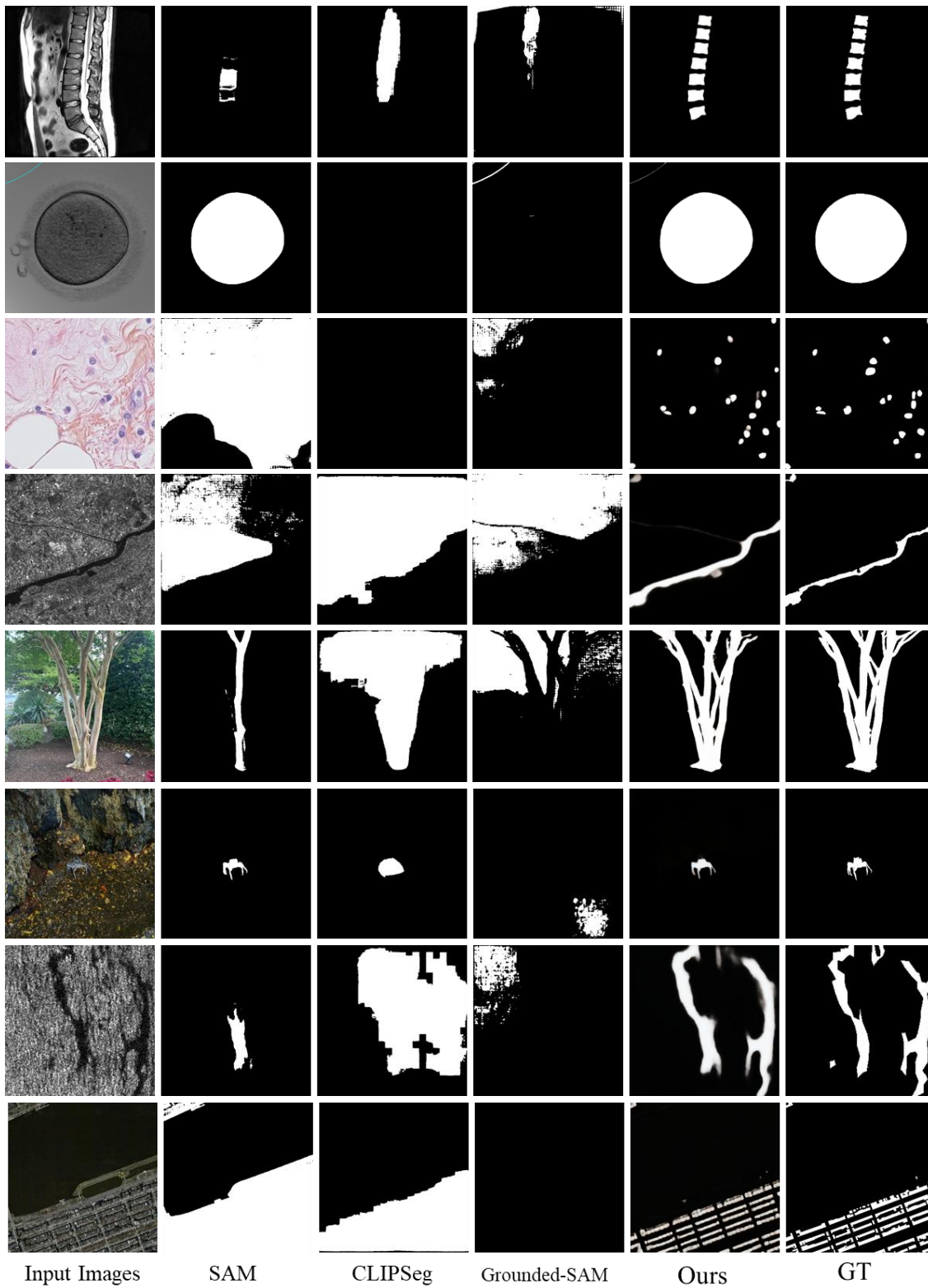


Figure 13. More visualization results for the image matting task.





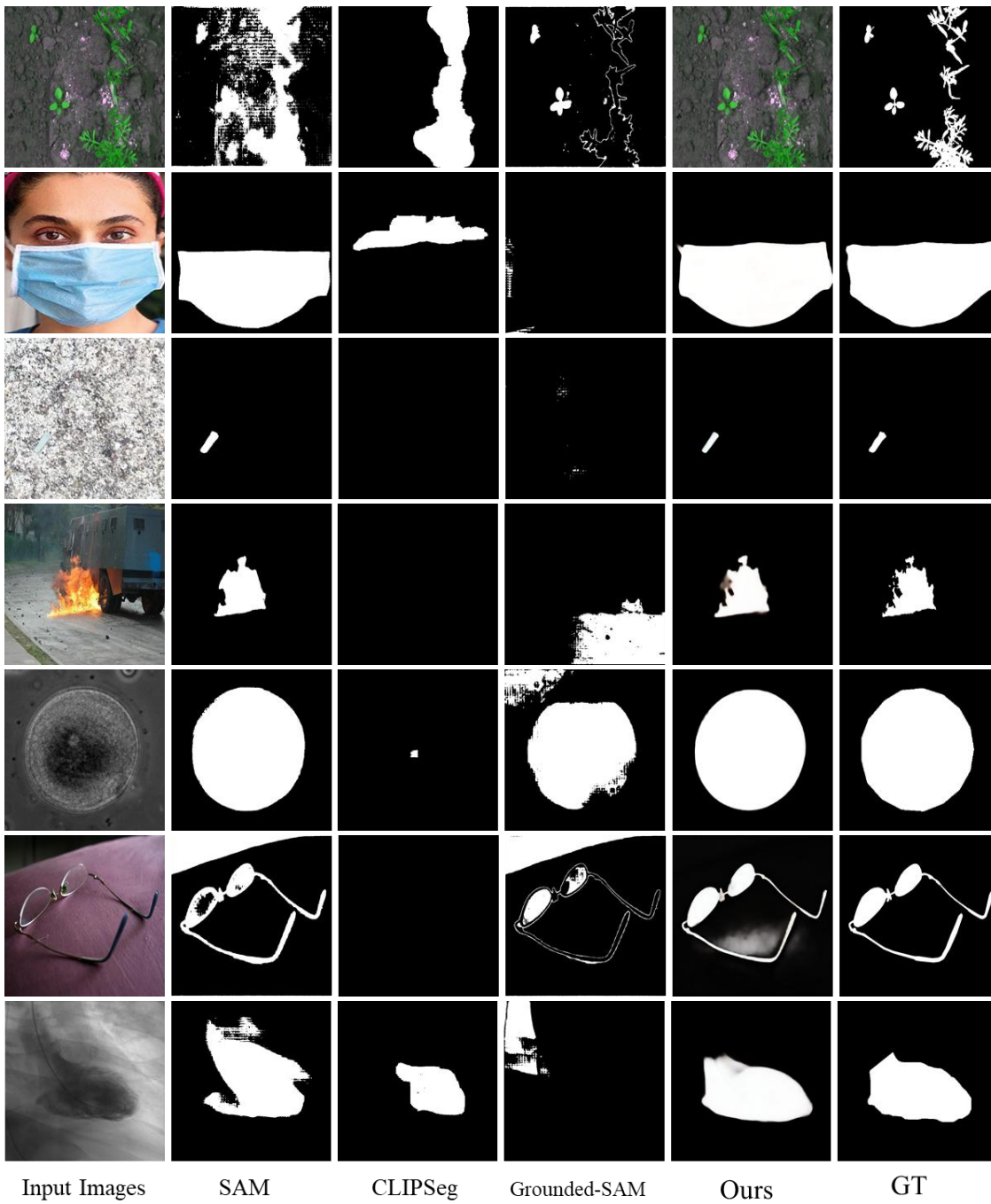


Figure 14. More visualization results for numerous practical downstream applications.